

---

Wesleyan University

---

A BLACK HOLE AND A STARBURST  
WALK INTO A BAR:  
UNMIXING AND DILUTING EMISSION LINE  
COCKTAILS SERVED IN THE LOCAL UNIVERSE

by

Sophia Flury

A thesis submitted to the  
faculty of Wesleyan University  
in partial fulfillment of the requirements for the  
Degree of Master of Arts

---

Middletown, Connecticut

---

---

May 2018

---

---

Who understands the world, and when  
Will he make it make sense? Or she?

Maybe there is a pair of them, and they sit  
Watching the cream disperse into their coffee

Like the A-bomb. *This equals that*, one says,  
Arranging a swarm of coordinates

On a giant grid. They exchange smiles.  
It's so simple, they'll be done by lunchtime,

Will have the whole afternoon to spend naming  
The spaces between spaces, which their eyes

Have been trained to distinguish. Nothing  
Eludes them. And when the nothing that is

Something creeps toward them, wanting  
To be felt, they feel it. Then they jot down

Equation after equation, smiling to one another,  
Lips sealed tight.

— “Life on Mars”, Tracy K Smith

---

# Acknowledgements

---

I must go down to the seas again, to the lonely sea and the sky,  
And all I ask is a tall ship and a star to steer her by;  
And the wheel's kick and the wind's song and the white sail's shaking,  
And a grey mist on the sea's face, and a grey dawn breaking.

— “Sea Fever”, John Masefield

---

As astronomers know all too well from the history of classification in our discipline, prescribing a discrete set of noumena for that which we observe or experience rarely works in practice. So it is with those the author wishes to thank. Bearing that in mind, Reader, the people deserving the author's gratitude fall largely into two groups: the shipwrights and the navigators. Neither is any more or less significant than the other, and both are necessary for a voyage. The author will proceed with this analogy as best as possible.

## **The Shipwrights**

The author's personal journey while producing this body of work has been complex. She could not have embarked on or completed this without the love and support of some incredible people whose tireless efforts served to build her a “tall ship” to carry her through this immense project and a “star to steer her by”. Her parents and brother saw her through time in the hospital, cared for her

during an incapacitating illness, and have come to embrace her as their daughter and sister. Her best friend, Maria, with her countenance and compassion (and admittedly warranted criticisms), carried her through trauma, coming out, and self actualization. Even with the demands of an infant, her dear friend Jon and his partner Ana took a substantial part of their time and energy to help her through illness, begin her transition, and embark on this voyage. These friends and family have all additionally humored her by enduring her ceaseless rambling about this project with immense patience.

Annie, a personal mentor, taught the author to embrace her scientific mind and passion for exploration in the wake of trauma, “to let the soft animal of [her] body love what it loves”. The members of the Almost Uptown Poetry Cartel, notably Marty and Gillian, taught her to “sound [her] barbaric yawp over the roofs of the world”, to “suck out all the marrow of life”, to express her vision of the universe unabashed. It was at Marty’s behest that she incorporated the epigraphs.

Though they themselves had great undertakings over the past two years, Evan and Prajwal helped her to plot her own course through this project. Through late nights, failed code, and dead ends, she has shared in their frustrations and successes and received their kind support. Jessica and Ismael have, in their own ways, expressed support for the author both in her scientific work and in her personal wellbeing throughout this project.

There are others who have contributed substantially to her growth and ability to complete this project, and an exhaustive list is not possible. Danielle offered solidarity in the author’s struggles with illness and trauma and provided unending support in coming out and beginning to transition. Sheenna worked with the author on developing confidence in her research and pride in her science results.

With their somewhat unorthodox beliefs, Ericka and Jennelle helped the author to maintain an opened mind, to embrace the unknown, and to consider emergence over reductionism as a more holistic scientific philosophy.

### **The Navigators**

The author's academic career has been and continues to be indirect. While attempting to understand where she is and where she would like to go, there have been some brilliant and nurturing mentors in the author's life who have helped her to navigate the "wheel's kick" and "grey mist" she encountered during the course of this project.

Chris Bradley once said to the author that majoring in physics was "a waste of talent". Nonetheless, Chris nurtured in her an intimate relationship with poetry that has simultaneously tethered and inspired her study of physics and astronomy over the past decade.

Six years ago, Catrina Hamilton-Drager sent the author off to this institution after her direct guidance of the author's studies at Dickinson College. In that subsequent time, she continued to help the author understand and set professional goals while grounding her in her own humanity. Catrina's continuing support has empowered the author to strive for both excellence and compassion during this project.

The faculty and staff of this department deserves thanks. Linda provided substantial support with organizing important non-scientific details, particularly funding for conferences and somewhat banal elements of the day-to-day. She also brought an important human element to the author during the project that brought life context to the project, for which the author is immeasurably grateful. Bill and Meredith took substantial time to do independent tutorials with the

author over the summer, which gave her invaluable astrophysical insight and techniques which appeared in this project in the forms of radiative processes and stellar population synthesis. Meredith additionally offered guidance in navigating some particularly tumultuous epochs of the project. Roy gave her much-needed technical support with hardware and software, especially in compiling the **MAPPINGS** and **STARBURST99** codes, which drastically improved her modeling capabilities even beyond the scope of this thesis. Seth pointed the author to resources for ISM physics (notably the Draine text to supplement that of Osterbrock and Ferland) and the Montreal White Dwarf Database, the latter which proved significant in her pAGB stellar population synthesis expanding on models by Binnette (1994) that ultimately could not be included in this body of work.

## O Captain! My Captain!

---

O Captain! my Captain! our fearful trip is done,  
The ship has weather'd every rack, the prize we sought is won,  
The port is near, the bells I hear, the people all exulting,  
While follow eyes the steady keel, the vessel grim and daring.

— “O Captain! My Captain!”, Walt Whitman

---

It is only with the guidance of her adviser, Ed Moran, that her “ship has weather’d every rack”. His deep insight often came from balancing his childlike excitement with patient skepticism. This challenged the author to channel her eagerness into a thorough and empiric framework without losing sight of the joy which accompanies a moment of discovery. Often, she liked to envision her frequent research meetings with Ed as the introductory epigraph depicts: smiling knowingly over coffee, ideas wafting through the air. While coffee was in abundance, no breakthroughs came so readily as the poem might imply. And the shared excitement over each progression was unbridled by comparison.

His encouragement to take intellectual risks in the context of research, to explore new ideas and challenge the old, often blurred the line between navigator and shipwright. While often reining in the author’s eagerness to venture into uncharted territory, Ed would also gently point her in the right direction, at once both a star and a steady keel. At the same time, he actively instilled in her a courage and confidence in her scientific conclusions to the extent that she has developed an excitement for sharing her ideas with the scientific community. The author could not have asked for a more insightful, caring, and thoughtful mentor.

# Contents

<b>1</b>	<b>A Bird for the Auger</b>	<b>1</b>
<b>2</b>	<b>To Stir Things Apart</b>	<b>8</b>
2.1	Fractional Weights . . . . .	9
2.2	Simple Mixing Model . . . . .	11
2.3	Technique for Solving the Model . . . . .	12
<b>3</b>	<b>Balancing the Weighbridge</b>	<b>16</b>
3.1	Constraints on the H II Locus . . . . .	17
3.2	Constraining AGN Fraction . . . . .	24
3.3	Demonstration of Method . . . . .	27
<b>4</b>	<b>The Purpose Breaks</b>	<b>31</b>
4.1	Fruit from the Integral Field . . . . .	32
4.1.1	The S7 IFU Data . . . . .	33
4.1.2	Decomposition Test Samples . . . . .	34
4.2	Reification . . . . .	36
4.2.1	Decomposition Predictions . . . . .	39
4.2.2	Beyond the Aperture . . . . .	45
<b>5</b>	<b>Intricate Ropes</b>	<b>47</b>
5.1	Published Values . . . . .	48



5.2	Electron Density . . . . .	50
5.3	Electron Temperature . . . . .	53
5.4	Gas Pressure . . . . .	54
5.5	Chemical Abundance . . . . .	55
5.5.1	Computing Oxygen Abundance . . . . .	56
5.5.2	Cooling and Evolution Sequences . . . . .	59
5.5.3	Total Abundances . . . . .	61
5.6	Dust . . . . .	62
5.7	Additional Parameters . . . . .	66
5.8	Ionizing Continuum . . . . .	67
<b>6</b>	<b>The Purpose Holds</b>	<b>70</b>
6.1	Simulating Single-Aperture Observations . . . . .	71
6.2	Effective Ionization Parameter . . . . .	74
6.3	Dilute Mixing Sequence . . . . .	76
6.4	Second Coming . . . . .	78
<b>7</b>	<b>But After All</b>	<b>82</b>
	<b>Bibliography</b>	<b>86</b>

# Chapter 1

## A Bird for the Auger

---

“Omens are wont,” said Janus, “to wait upon beginnings.  
At the first word ye prick up anxious ears;  
from the first bird he sees, the auger takes his cue.”

— *Fasti*, Ovid

---

Fath’s spectroscopic investigation of “spiral nebulae” in 1908 led him to discover that gaseous nebulae and galaxies often have similar emission features, specifically noting the [OIII]  $\lambda\lambda 4959, 5007$  doublet and unresolved [OII]  $\lambda\lambda 3726, 3729$  doublet in NGC 1068. He concluded that “it is wholly inadequate to answer the question as to the real nature of these interesting objects.” Seyfert followed up on NGC 1068 in his seminal 1943 paper on several spiral galaxies, finding again the extreme prominence of [OII] and [OIII] lines, along with a wealth of other emission features from the nuclear regions including Doppler-broadened high-velocity ( $3600 \leq v \leq 8500 \text{ km s}^{-1}$ ) recombination lines (primarily H $\alpha$   $\lambda 6563$  and H $\beta$   $\lambda 4861$ ), the auroral [OIII]  $\lambda 4363$  line<sup>1</sup>, the [NII]  $\lambda\lambda 6548, 6583$ , [SII]  $\lambda\lambda 6716, 6731$ , and [OI]  $\lambda\lambda 6300, 6363$  doublets, HeII  $\lambda 4686$ , and multiple iron coronal lines. He compared these to the H II region “knots” in spiral disks and suggested that the primary distinction between the nuclear and non-nuclear sources is the “evidence of widening of the lines” since they otherwise appeared equally bright and simi-

---

<sup>1</sup>Fath may have detected this, but it is unclear in his publication whether this feature is [OIII] or the nearby recombination line H $\gamma$   $\lambda 4340$ .

larly ionized, implying what is now known: the mechanism of photoionization is at play in both phenomena.

Flux-ratio plots like optical “BPT” diagnostics (Baldwin, Philips, and Terlevich 1983, Veilleux and Osterbrock 1987; henceforth VO87) can be quite successful at distinguishing between Seyfert narrow-line regions (NLR) and star-forming regions. These diagnostics use ratios of fluxes of emission lines produced by collisionally excited states in ions like [OIII] and [NII] to those from ion-electron recombination such as  $H\alpha$  and  $H\beta$ . Comparing these flux ratios gauges the relative degree of ionization in a gaseous nebula and offer an empirical means with which to segregate sources of excitation such as an accreting massive black hole (MBH), shocks, and early-type main sequence stars. While the flux-ratio diagnostic plots are empirical, ionization models provide deeper insight into the underlying physical mechanism, allowing us to interpret the fundamental nature of these self-segregating objects. However, flux from nebulae powered by accreting MBHs in galactic nuclei can sometimes be combined with emission from star-forming regions in the spectroscopic aperture, though, which complicates classification and interpretation. With the addition of continuum starlight, this effect can render the source of ionization ambiguous. This notion of “composite” emission-line galaxies is not a new one—the possibility of Seyfert-like nuclei “hidden” by H II regions has been a topic of interest for nearly four decades (first proposed by Véron et al. 1981).

In their exploration of the ionizing mechanisms of low-ionization nuclear emission-line regions (LINERs; Heckman 1980)<sup>2</sup> in the Palomar magnitude-limited galaxy

---

<sup>2</sup>LINERs are still not universally understood (see, e.g., Filippenko 2003 and references therein). Some of the most successful LINER explanations are, in no particular order, an ensemble of post asymptotic giant branch (pAGB) stars and pre-degenerate central stars of planetary nebulae (e.g., Binnette 1994, Yan and Blanton 2012), shocks or gas flows (e.g., Heckman 1989, Rich et al. 2010), or even low-luminosity AGN (e.g., Ferland and Netzer 1983, Eracleous, Hwang,

survey, Ho, Filippenko, and Sargent (1993, henceforth HFS93) discovered that potentially composite nuclei reside in distinct locations in diagnostic diagrams determined largely by low-ionization collisional lines like [NII], [SII], [OII], and [OI], which are stronger relative to  $H\alpha$  than expected for H II regions but weaker than those of LINERs. Dubbing these composites “transition” objects, they found that this subset of galactic nuclei contains blue starlight continua characteristic of star formation and suggested these galaxies are LINER-starburst composites. In their release of the spectroscopic results from the Palomar survey, Ho, Filippenko, and Sargent (1997) demonstrated the first statistical constraint on the frequency of composites:  $\sim 16\%$  of line-emitting galaxies (65 of the total 418) are composite while only 12% (52 of 418) are found to be classical Seyferts. If composites all contain AGN, this would more than double the number of accreting MBHs in the survey. They also demonstrated that composites straddle the theoretical demarcations between H II regions and LINERS, as shown in Figure 1.1, complicating diagnostic classification.

More recently, work by Kewley et al (2001; henceforth Ke01), Kauffmann et al. (2003; henceforth Ka03) and Kewley et al. (2006; henceforth Ke06) utilized ensembles of photoionization models and the preliminary results of the Sloan Digital Sky Survey (SDSS) in the BPT diagnostic to examine in dramatically improved detail the populations of AGN and star-forming regions. Of the 85224 galaxies contained in the culminating work by Ke06, 5870 (7%) were classified as composite objects, more than twice the frequency at which classical Seyferts occur and similar to the rate at which LINERs occur. They presume that these composites contain a mix of emission from high metallicity H II regions and AGN, and Flohic 2010). Given the relative success of each of these interpretations, LINERs are, in all likelihood, a heterogeneous class of objects.

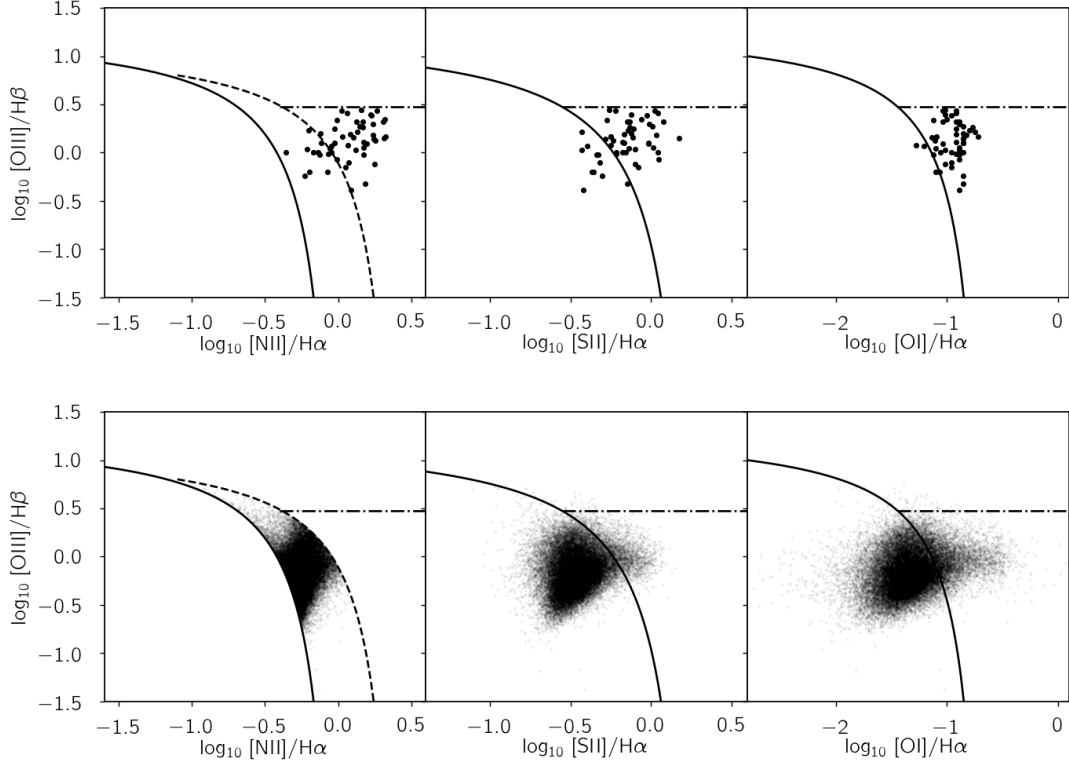


**Figure 1.1:** Diagnostic flux-ratio diagrams for composite galaxy samples from *top*: Ho, Filippenko, and Sargent (1997) and *bottom*: the Portsmouth analysis of the SDSS legacy data (Thomas et al. 2013) according to criteria from Kewley et al (2006). Solid lines are the Kauffmann et al. (2003) [NII] and Kewley et al. (2001) [SII] and [OI] demarcations, dashed the Kewley et al. (2001) [NII] demarcation, and dot-dashed the classical  $[\text{OIII}]/\text{H}\beta = 3$  cutoff for Seyferts.

ascribing the composite classification to the abundance sensitivity of the [NII] emission for the star-forming locus in the primary BPT diagnostic, which compares  $[\text{OIII}]\lambda 5007/\text{H}\beta$  (sensitive to ionizing intensity) to  $[\text{NII}]\lambda 6583/\text{H}\alpha$  (sensitive to metallicity and the extent of the partially ionized part of a nebula). However, they also find that these objects tend to fall within the H II locus in the other two BPT diagnostic plots, making their supposition somewhat tenuous. Furthermore, they themselves admit, as HFS93 proposed before, the potential for an amalgam of LINER-starburst emissions in the case where the former is not powered by a

BH, complicating efforts to obtain a true census of MBHs.

Alternative attempts to determine whether AGN exist in these enigmatic composite nuclei have relied heavily on multi-wavelength observations in the X-ray, infrared, and radio regimes (e.g., Hill et al. 2001, Seth et al. 2008, Sartori et al. 2015, Kirkpatrick et al. 2016, Koss et al. 2017). However, the signature of the presence of a MBH can be difficult to detect, especially if a starburst is also powerful enough to produce emission within these bands, making this approach biased towards detecting particularly powerful AGN and thus incapable of consistently demonstrating whether an AGN is associated with the observed nebula. Indeed, it has been shown that starburst emission could “hide” AGN signatures in low spatial resolution spectra with 15 - 30% of a local host galaxy filling the SDSS 3'' spectral aperture (e.g., Kewley, Jansen, and Geller 2005, Trump et al. 2015).

First proposed by Véron et al. (1981), the  $\text{HeII}\lambda 4686/\text{H}\beta$  flux ratio can be used to infer the presence of an accreting MBH. Studies of Wolf-Rayet (WR) starbursts, such as Brinchmann, Kunth, and Durret (2008) and Shirazi and Brinchmann (2012; henceforth SB12), have used a  $\text{HeII}/\text{H}\beta$  criterion to reject objects possibly contaminated by AGN. Combining a sample of WR galaxies and photoionization modeling, SB12 found that even the strongest star formation can, at most, produce  $\text{HeII}/\text{H}\beta \approx 0.1$ . Additional work on the ionizing power of intermediate mass black holes (IMBHs) by Ludwig et al. (2012) found that the flux of HeII tends to be at least 10% that of  $\text{H}\beta$ . Combined with the work by SB12, this might suggest that  $\text{HeII}/\text{H}\beta = 0.1$  represents a rough demarcation between AGN and WR starbursts.

Together, these explorations prompted subsequent studies into the use of HeII to tease out the presence of a MBH; however, these focused primarily on low-metallicity candidates (e.g., Sartori et al. 2015, Bär et al. 2017, Kawasaki et al.

2017) or confirming multiwavelength detections (e.g., Koss et al. 2017) rather than resolving the composite hypothesis. SB12 additionally proposed, as others before them (e.g., Hill et al. 2001, Ke01, Ke06) that the observed emission lines in composite galaxies are a linear combination of AGN and H II emission-line spectra. However, they did not test this supposition, which has since remained in the realm of hypothesis insofar as single spectroscopic apertures are concerned.

Long-slit spectroscopy at high enough angular resolution ( $1''$  from the ground) has offered the first spatial glimpse into composite objects but is ultimately one-dimensional (e.g., Bennert et al. 2006). With the advent of integral field unit (IFU) spectroscopy, a number of efforts have been made to further deconstruct the amalgam of emission in the central kiloparsec of nearby ( $z < 0.02$ ) galaxies by spatially resolving the individual components over a sizable field of view (e.g., Davies et al. 2007, Dopita et al. 2014, Davies et al. 2014a,b, Davies et al. 2016a,b, Davies et al. 2017). Such explorations have revealed separate Seyfert and starburst components that often appear to be linear combinations of nebular emissions from two (or more) distinct sources of emission-line flux. But these endeavors have provided no means of addressing the ambiguity of single-aperture spectroscopy of nuclear composite galaxies without costly, extensive IFU observations.

It is our aim to address the composite hypothesis more directly so that IFU and multiwavelength approaches are unnecessary for determining the presence of a MBH. Using constraints of empirical trends from readily observed properties in the SDSS, we establish a method for decomposing the constituent emission-line sources responsible for composite objects and compare our predictions against IFU data in a rigorous proof of concept before applying the technique to a sample of ambiguous HeII - selected galaxies. The empirical rather than theoretical foundations allow our predictions to be independent of the assumptions necessary

---

for a model-based approach. High quality IFU spectroscopy offers the unique opportunity to demonstrate the effectiveness of our method while offering significant insights into the complexity of mixing emission-line fluxes from two different sources. Application to additional samples suggests both the need for future observations and a broader scientific context for our technique.



## Chapter 2

### To Stir Things Apart

---

Thomasina: When you stire your rice pudding, Septimus, the spoonful of jam spreads itself round making red trails like the picture of a meteor in my astronomical atlas. But if you stir backwards, the jam will not come together again. Indeed the pudding does not notice and continues to turn pink just as before. Do you think this odd?

Septimus: No.

Thomasina: Well, I do. You cannot stir things apart.

— *Arcadia*, Tom Stoppard

---

Before we go about testing the composite hypothesis, we need to establish a quantitative formalism with which to frame our expectations for composite flux ratios. We begin as simply as possible, assuming that the AGN and star formation emissions add in a linear fashion, as suggested by previous work (e.g., Hill et al. 2001, Ke01, Ke06, SB12). Each source’s emission lines are weighted according to their fractional contribution to the observed “composite” lines with the necessary requirement that the weights sum to unity. We apply this concept to diagnostic emission-line flux ratios, expressing the observed flux ratio in terms of the ratio of weighted sums of the putative source fluxes.

These expressions can be rewritten to solve for two parameters: the position of a predicted star forming component on the BPT diagnostic diagram (see Figure 2.1) and the fractional contribution of assumed AGN emission to the observed

line flux. What this requires in addition to an observed composite emission-line spectrum, however, is a presupposed set of line ratios characteristic of the AGN component which, according to the composite hypothesis, occurs simultaneously with star-forming regions in the spectral aperture. We approach this problem with a Monte Carlo method in which we generate tens of thousands of pairs of flux ratios in the region of the BPT diagram which is solely characteristic of AGN, each pair representing the AGN contribution to the composite flux. With each assumed pair of flux ratios, we use the observed composite flux ratios and the explicit formalism to infer both the starburst contribution to the composite and the fractional weights.

While we are now able to rapidly solve our linear composite mixing model for all the constituent components, the Monte Carlo approach leaves us with thousands of quantitatively viable solutions to examine. Solely within the context of our current formalism, none of these results are demonstrably more probable than any other. Indeed, we must invoke some additional means by which to assess the success or failure of this composite hypothesis.

## 2.1 Fractional Weights

We define the emission fraction  $f_{SF}$  of total, pure star-forming emission-line flux ( $F_{SF}$ ) present in the composite emission-line flux  $F$  such that

$$f_{SF} = \frac{F_{SF,comp}}{F_{SF}} \quad (2.1)$$

and the emission fraction  $f_{AGN}$  of total, pure AGN narrow emission-line flux ( $F_{AGN}$ ) present in the observed emission-line flux  $F_{tot}$  such that

$$f_{AGN} = \frac{F_{AGN,comp}}{F_{AGN}}, \quad (2.2)$$

where  $F_{SF,comp}$  and  $F_{AGN,comp}$  are the respective contributions by star-forming and AGN narrow-line regions to the composite emission. The sum of  $f_{SF}$  and  $f_{AGN}$  independent of the flux terms, however, is unknown. This sum need not be unity since the AGN NLR emission line luminosities could be more extinguished than the HII regions within the spectral aperture<sup>1</sup>. We make some simple, common assumptions to address this unknown.

In practice, it is often convenient and useful to write the line luminosities relative to  $H\beta$ , meaning that, for all intents and purposes in the context of flux-ratio diagnostics,  $H\beta = 1$  and  $H\alpha = R$ ,  $R$  being the observed Balmer decrement. When we consider luminosities for  $H\alpha$  and  $H\beta$ , we can write

$$f_{SF}^{\alpha} R_{SF} + f_{AGN}^{\alpha} R_{AGN} = R \quad (2.3)$$

and

$$f_{SF}^{\beta} + f_{AGN}^{\beta} = 1 \quad (2.4)$$

with  $\alpha$  indicating the fraction in lines near  $H\alpha$  and  $\beta$  indicating the fraction in

---

<sup>1</sup>There is no way, from a single-aperture observation, to infer whether the objects are physically co-spatial or, instead, visibly coincident within the aperture. If physically coincident, one might assume flux from multiple sources is similarly affected by attenuation; however, the components might simply be visibly coincident within the aperture of the observation and thus might be subject to different degrees of extinction. If the components' velocities relative to the line of sight differ significantly enough to be detected within the spectral resolution of the instrument, the emission lines from the two (or more) sources will be distinct and separable, allowing us to determine and compare the relative degrees of reddening.

lines near  $H\beta$ .

If we assume that the extinction of nebular emission from HII regions and the NLR is identical, the Balmer decrement term drops out, giving both

$$f_{AGN}^{\alpha} = f_{AGN}^{\beta} = f_{AGN} \quad (2.5)$$

and

$$f_{SF}^{\alpha} = f_{SF}^{\beta} = f_{SF}, \quad (2.6)$$

subsequently yielding

$$f_{AGN} + f_{SF} = 1 \quad (2.7)$$

which significantly simplifies our model.

## 2.2 Simple Mixing Model

We assume that the composite object's emission spectrum is a weighted sum of emission from star-forming regions in the galaxy and a hosted AGN. This implies that the sum of the fraction of the HII and AGN luminosities accounts for the total observed flux  $F_{tot}$  such that

$$f_{SF} \frac{F_{SF}}{F_{tot}} + f_{AGN} \frac{F_{AGN}}{F_{tot}} = 1. \quad (2.8)$$

This is necessarily true because, according to the definitions above,

$$f_{SF} F_{SF} + f_{AGN} F_{AGN} = F_{SF,comp} + F_{AGN,comp} = F_{tot}. \quad (2.9)$$

From what we have derived thus far, we write a general expression for composite flux ratios such that

$$\frac{F_{\lambda_1}}{F_{\lambda_2}} = \frac{(1 - f_{AGN})F_{\lambda_1,SF} + f_{AGN}F_{\lambda_1,AGN}}{(1 - f_{AGN})F_{\lambda_2,SF} + f_{AGN}F_{\lambda_2,AGN}} \quad (2.10)$$

for any emission line fluxes  $F_{\lambda_1}$  and  $F_{\lambda_2}$  which have been measured from the composite candidate's starlight-subtracted spectrum and corrected for extinction, with the subscript  $SF$  symbolizing emission contributed by the hypothetical H II region and the subscript  $AGN$  the hosted pure AGN. For the primary BPT diagnostic diagram flux ratios, Equation 2.10 becomes

$$\frac{[\text{NII}]}{\text{H}\alpha} = \frac{f_{SF}[\text{NII}]_{SF} + f_{AGN}[\text{NII}]_{AGN}}{f_{SF}\text{H}\alpha_{SF} + f_{AGN}\text{H}\alpha_{AGN}} \quad (2.11)$$

and

$$\frac{[\text{OIII}]}{\text{H}\beta} = \frac{f_{SF}[\text{OIII}]_{SF} + f_{AGN}[\text{OIII}]_{AGN}}{f_{SF}\text{H}\beta_{SF} + f_{AGN}\text{H}\beta_{AGN}}. \quad (2.12)$$

The  $[\text{OIII}]$ ,  $[\text{NII}]$ ,  $\text{H}\alpha$ , and  $\text{H}\beta$  terms signify the flux of the identified emission lines.  $[\text{OIII}]$  in this instance is only the stronger line of the doublet,  $\lambda 5007$ , as is  $[\text{NII}]$  from its doublet,  $\lambda 6583$ .

### 2.3 Technique for Solving the Model

Solving Equations 2.11 and 2.12 for  $f_{AGN}$  using Equation 2.7, we find the following two definitions:

$$f_{AGN} = \frac{[\text{NII}]/\text{H}\alpha_{SF} - [\text{NII}]/\text{H}\alpha}{[\text{NII}]/\text{H}\alpha_{SF} - [\text{NII}]/\text{H}\alpha_{AGN}} \quad (2.13)$$

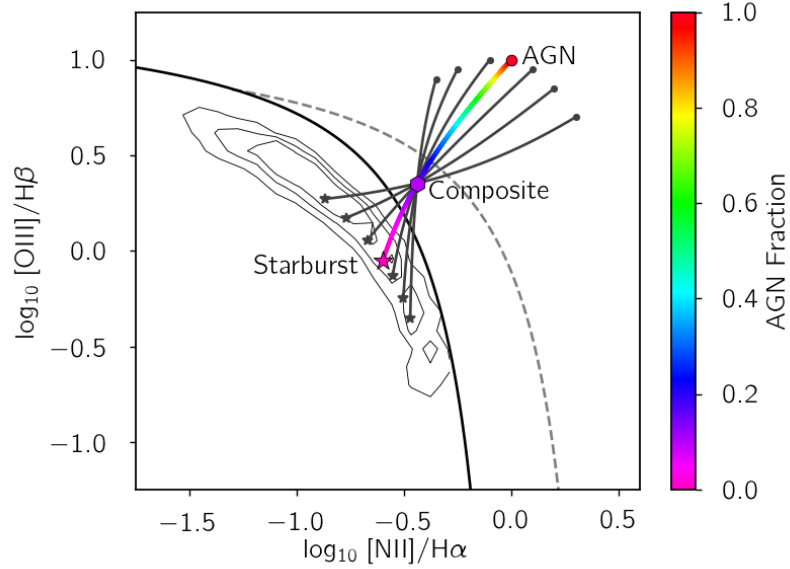


**Figure 2.1:** Example of a sequence of line ratios for  $f_{AGN}$  ranging from 0 to 1 (color-gradient line) in the primary ( $[NII]/H\alpha$ ) BPT diagnostic diagram. The putative AGN and starburst components are shown as a circle and star, respectively, and are colored according to the appropriate  $f_{AGN}$ . A composite having a 15% AGN contribution mixed linearly with the starburst component is shown as a hexagon and is colored according to the AGN fraction. Dark grey lines are additional mixing solutions for the composite for a range of AGN fractions and locus positions, demonstrating the need for constraints. Solid black line is the Ka03 demarcation, dashed grey line the Ke01 upper limit to starburst line ratios. Black contours represent the distribution of HII galaxies defined in Chapter 3.

and

$$f_{AGN} = \frac{[OIII]/H\beta_{SF} - [OIII]/H\beta}{[OIII]/H\beta_{SF} - [OIII]/H\beta_{AGN}}. \quad (2.14)$$

Taking the difference between Equations 2.13 and 2.14, knowing that Equation 2.5 requires this difference to be zero, allows us to determine the flux ratios for a composite or one of its components given the other two line ratios, fully independent of AGN or starburst fraction.

Because we know the H II  $\log [NII]/H\alpha$  ratios as a function of its  $\log [OIII]/H\beta$  (see Equation 3.1 and Figure 3.1 in Chapter 3), finding the latter will inherently

give us the former. For any presumed AGN line ratios and an observed potential composite, we can infer the flux ratios of the H II component (see Figure 2.1 and Equation 3.1) using the difference of Equations 2.13 and 2.14, which implies any assumed pair of AGN flux ratios will correspond to a unique mixing solution for the composite candidate. We implement a bisection root-finding method in `python` to minimize the difference in order to infer the star formation component which satisfies the condition  $f_{AGN}^{\alpha} = f_{AGN}^{\beta}$ . The procedure necessarily excludes the asymptotic solution in which the AGN and star-forming regions have the same line ratios since root-finding methods can converge on an asymptote rather than a real solution. Our bisection method typically converges on the satisfying HII flux ratios in less than ten iterations. Upon finding the HII locus position, we can use Equations 2.13 and 2.14 to obtain the fraction of AGN emissions contributing to the composite candidate.

In order to compute this star-forming component, we must assume the flux ratios of the putative AGN contribution without any genuine knowledge of what those might be. As such, we implement a Monte Carlo approach by sampling  $\sim 2.5 \times 10^4$  uniformly random pairs of flux ratios in BPT space above the Ke01 theoretical maximum starburst line. We apply our root finding method to the observed “composite” galaxy and each sampled pair of flux ratios to obtain a corresponding set of AGN fraction and H II locus position values. Because the bisection routine converges rapidly on each solution, it is not computationally cumbersome to apply it to some  $10^4$  scenarios<sup>2</sup>. This is all well and good, but there are now tens of thousands of unique solutions and no way of knowing which are most probable!

---

<sup>2</sup>For a contemporary desktop computer, our Monte Carlo method takes about 30 seconds to run for a single object. Applied to all 5870 composites reported by Ke06, this would take just over two days.

To assess the viability of each of these numerous results, we winnow out any Monte Carlo line ratios which yield  $f_{\text{AGN}} \notin (0, 1)$ . The degree to which this reduces the solution count can vary from object to object but is, at best, only able to reduce the number of results by a factor of 10 and thus not demonstrably sufficient in determining the best solution. Additional insight is needed to say with certainty which, if any, of these results are viable explanations of the observed composite-classified line ratios. We are reluctant to introduce further assumptions required by more rigorous modeling and instead take a more empirical approach to resolving the large number conundrum.



## Chapter 3

### Balancing the Weighbridge

---

The 56 lb. weight. A solid iron  
Unit of negation. Stamped and cast  
With an inset, rung-thick, moulded, short crossbar

For a handle. Squared-off and harmless-looking  
Until you tried to lift it, then a socket-ripping,  
Life-belittling force –

Gravity’s black box, the immovable  
Stamp and squat and square-root of dead weight.  
Yet balance it

Against another one placed on a weighbridge–  
On a well-adjusted, freshly greased weighbridge–  
And everything trembled, flowed with give and take.

— “Weighing In”, Seamus Heaney

---

Outlined below is the empirical foundation with which we anchor our predictions about the two constituents of composite galaxies. Such an approach requires observation, often in the form of extensive surveys to enable large number statistics. The SDSS legacy survey provides such an opportunity, and thus we draw from it extensively to understand the fundamental components that we hypothesize are the building blocks of composites. The wealth of information contained in spectra regarding stellar populations and nebular structure of AGN NLR allow us to evaluate our predictions to determine which, if any, are physically likely.

To begin, we need to describe the distribution of starburst galaxies in the BPT

diagnostic diagram formally so that we can readily infer the starburst flux ratios from the mixing model. For this purpose, we define a sample of star-forming galaxies from the Moran et al. (2014) parent sample of SDSS galaxies. We describe the distribution of these galaxies in the primary BPT diagnostic diagram formally. Using results from our spectral fitting of the sample, we demonstrate the effectiveness of intrinsic  $g - r$  color as a constraint on the inferred locus position. From here, we look to alternate parent samples large enough to provide an AGN child sample for large-number statistics with the correlations of strong emission lines. With this large child sample, we show that emission-line tracers of extended nebular structure can be used as a constraint on the AGN fraction.

With two separate empirical constraints on the values inferred from the simple mixing model, we determine the likelihood any given pair of the assumed Monte Carlo flux ratios satisfies the simple composite mixing hypothesis. We examine results of an example composite galaxy as a demonstration of the use of empirical limits on the assumed flux ratios to establish the statistical component of our method, thereby laying the foundation for a rigorous test of concept.

### 3.1 Constraints on the H II Locus

We take galaxies from the SDSS seventh data release (DR7; Abazajian et al. 2009) distance-limited ( $d \leq 80$  Mpc) parent sample of Moran et al. (2014) which have [OI], [OIII],  $H\beta$ ,  $H\alpha$ , [NII], and both [SII] emission lines detected with amplitude over noise (A/N) greater than 2.5 and which fall below the Ke01 maximum starburst limits and the more conservative Ka03 demarcation in all three BPT diagnostic diagrams (meaning they are consistently classified as starburst galaxies). These constraints yield a sample of 2167 nuclear star-forming galaxies with high-quality data.

While the H II locus of starburst galaxies closely follows the trend predicted by Ka03 for  $[\text{NII}]/\text{H}\alpha$  and Ke01 for  $[\text{SII}]/\text{H}\alpha$  and  $[\text{OI}]/\text{H}\alpha$ , the SDSS galaxies in the locus with  $\log_{10}[\text{OIII}]/\text{H}\beta \lesssim 0$  deviate from these proposed demarcations. As demonstrated in Figure 3.1,  $[\text{OIII}]/\text{H}\beta$  decreases with respect to each of the other BPT diagnostic flux ratios down and to the left in all three diagrams. We adopt the traditional hyperbolic description for the upper part of the locus as Kewley et al. (2013) did with their photoionization models, which is given by their Equation 3. We also employ a parabolic term<sup>1</sup> in order to describe the tail effectively such that, rewritten in terms of  $[\text{OIII}]/\text{H}\beta$  and for each of the BPT flux ratios relative to  $\text{H}\alpha$ ,  $X/\text{H}\alpha$ ,

$$\log_{10} \left( \frac{X}{\text{H}\alpha} \right) = \frac{a}{\log_{10} \left( \frac{[\text{OIII}]}{\text{H}\beta} \right) + c} + b + d \log_{10} \left( \frac{[\text{OIII}]}{\text{H}\beta} \right)^2. \quad (3.1)$$

To fit the locus in the BPT diagnostic diagrams, we bin all four flux ratios— $[\text{OIII}]/\text{H}\beta$ ,  $[\text{NII}]/\text{H}\alpha$ ,  $[\text{SII}]/\text{H}\alpha$ , and  $[\text{OI}]/\text{H}\alpha$ —in increments of 0.05 dex, sampled with respect to  $\log_{10}[\text{OIII}]/\text{H}\beta \in [-1, 1]$ ,  $\log_{10}[\text{NII}]/\text{H}\alpha \in [-2, -0.5]$ , and  $\log_{10}[\text{SII}]/\text{H}\alpha \in [-1.5, -0.5]$ . We compute the median of each of the four log flux ratios for each bin that contains at least 25 galaxies<sup>2</sup>. We then fit the proposed empirical model to the medians using the Levenberg-Marquardt nonlinear least squares routine `curve_fit` from the python module `scipy.optimize` to obtain the results in Table 3.1, which we show in Figure 3.1 along with the bin medians and original data set.

<sup>1</sup>Note that this is different from the empirically motivated model of Brinchmann, Pettini, and Charlot (2008), which uses a second-order polynomial to describe the entire distribution of galaxies on the HII locus resulting from their analysis of the SDSS dr4. While written in terms of  $[\text{OIII}]/\text{H}\beta$  as ours happens to be, their model is not used exclusively to describe the apparent “tail” leading away from the upper branch to the lower left of the diagnostic.

<sup>2</sup>Unless otherwise stated, all binning for properties of the H II sample is subsequently done in this manner.

**Table 3.1:** Parameters from nonlinear least-squares fits of Equation 3.1 to H II loci in each of the BPT diagnostics.

$X/H\alpha$	$a$	$b$	$c$	$d$
[NII]	1.443	0.349	-1.476	-0.241
[SII]+	0.166	-0.237	-0.982	-0.461
[OI]	0.008	-1.490	-0.777	-0.830

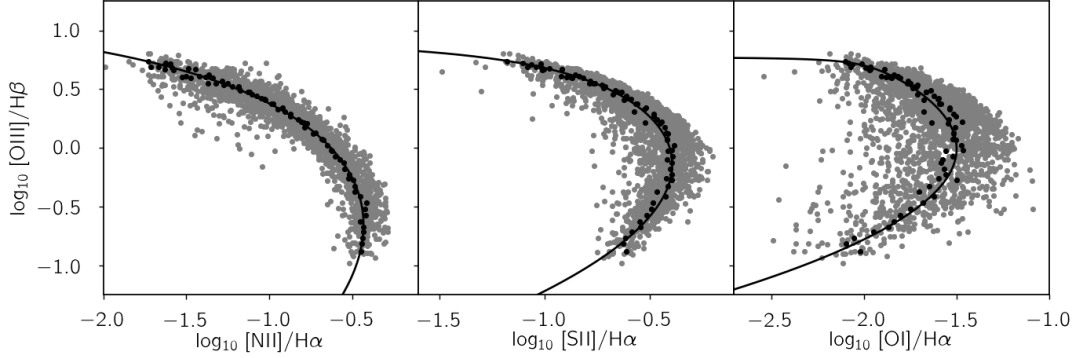


**Figure 3.1:** Description of the locus (black line) of H II galaxies (gray dots) binned in intervals of 0.05 dex in  $\log_{10}[\text{OIII}]/H\beta$ ,  $\log_{10}[\text{NII}]/H\alpha$ , and  $\log_{10}[\text{SII}]/H\alpha$  (black dots) in each of the BPT diagnostic plots.

We define the position of any given star-forming galaxy along this distribution in the primary BPT diagram as the point on the line of best fit to the locus for which the Euclidean distance between the fit and the object’s flux ratios is minimized. To make this position one dimensional, we compute the distance of this point from an arbitrary origin along the locus:  $\log_{10}[\text{OIII}]/H\beta = 0$ ,  $\log_{10}[\text{NII}]/H\alpha = -0.629$ . We implement a numerical root-finding algorithm to locate the pair of locus-position flux ratios and reduce the dimensionality to a single value.

With the H II locus position defined, we now look to determine the probability of each locus position inferred from the mixing model and assumed AGN flux ratios. In order to accomplish this, we compare the stellar populations of the composite candidate to those of H II galaxies with flux ratios in proximity to the

flux ratios of each predicted star-forming component. Historically, photometric color such as  $B - V$  has been used to determine the spectral type of stars in the absence of spectra. The SDSS DR7 archive provides the photometric magnitudes computed from images taken in all five Sloan bandpasses— $u$ ,  $g$ ,  $r$ ,  $i$ , and  $z$ —which have an effective wavelength coverage of 3500 to 9000 Å. The “fiber” magnitudes are computed from  $3''$  apertures placed at the same locations as the  $3''$  fibers used by the SDSS multi-object spectrograph. Because the photometry is often contaminated by emission lines and extinguished by dust local to the star-formation host galaxies, the observed fiber  $g - r$  color is not necessarily a good indicator of the true stellar population(s) associated with an extragalactic H II region.

To determine the intrinsic  $g - r$  color of the starlight contained within the SDSS spectral fiber, we turn to spectroscopy. We employ the **Gas AND Absorption Line Fitting** code (GANDALF; Sarzi et al. 2006) as discussed in Moran et al. (2014), which performs penalized pixel fitting developed by Cappellari and Emsellem (2004) and more rigorously implemented by Emsellem et al. (2004)<sup>3</sup> For continuum fitting, we use updated templates from the Medium-resolution Isaac-Newton Telescope Library of Empirical Spectra (MILES; Vazdekis et al. 2015), for which we have assumed a Kroupa initial mass function (IMF; Kroupa 2002), and solar abundances ( $[M/H]=0$ ). We assume the Calzetti extinction law (Calzetti 2001) to physically account for dust attenuation of starlight in these extragalactic star-forming regions. Figure 3.2 shows the intrinsic spectrum for four arbitrarily selected star-forming galaxies in our sample.

For ease of examining the stellar populations of all 2167 galaxies in our H II sample simultaneously, we process the synthetic stellar populations’ spectra

---

<sup>3</sup>The code implementing the penalized pixel fitting discussed in Cappellari and Emsellem (2004) is accessible through the open source software package **pPXF** available at <http://www-astro.physics.ox.ac.uk/~mxc/software/> in both **python** and **IDL**.

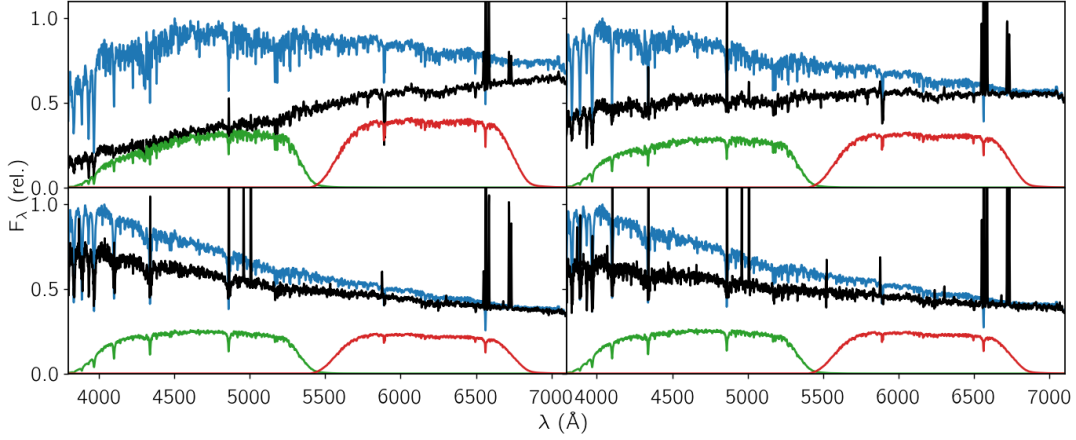


**Figure 3.2:** Four arbitrarily selected galaxies from the H II sample. Observed spectrum is shown in black, the ssp fits assembled from the MILES templates in blue, and the intrinsic starlight continuum as processed through  $g$ -band (green) and  $r$ -band filter transmission functions.

through the SDSS transmission functions for the  $g$ - and  $r$ -band filters<sup>4</sup> and convert to AB magnitudes. Following from Equation 7 in Fukigita et al. (1996), this is done by first convolving the ssp spectral flux  $\lambda F_\lambda$  with the appropriate transmission function  $G(\lambda)$  (see Figure 3.2) and normalizing by the wavelength-weighted transmission function such that

$$F_{\text{band}} = \int \lambda F_\lambda G(\lambda) d\lambda \left( c \int \lambda^{-1} G(\lambda) d\lambda \right)^{-1} \quad (3.2)$$

in units of flux density. From Equation 1 in Oke and Gunn (1983) and Equations 1-2 in Fukugita et al. (1996), we find the AB  $g$ - and  $r$ -band magnitudes using the relation

$$m = -2.5 \log_{10} \left( \frac{F_{\text{band}}}{3161 \text{ Jy}} \right). \quad (3.3)$$

We then compute the corrected  $g-r$  color by taking the difference of the computed  $g$ - and  $r$ -band magnitudes. We assume from here on that, in addition to the H

<sup>4</sup>Available at <http://classic.sdss.org/dr7/instruments/imager/>.

II galaxies, any composite candidate's color has been corrected in this manner unless otherwise stated.

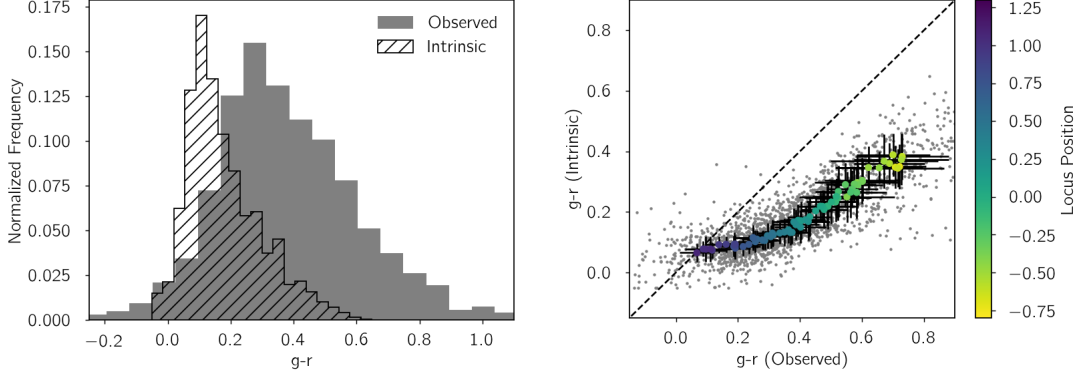


**Figure 3.3:** Comparison of the photometric and intrinsic  $g-r$  colors. *Left:* Distributions of the photometric fiber  $g-r$  (solid grey) and intrinsic ssp  $g-r$  (hashed). The latter is demonstrably more narrow and blue than the former. *Right:* Intrinsic vs photometric  $g-r$  (grey dots) with the peak of the distribution highlighted by taking the median of each  $g-r$  color sampled from bins drawn with respect to locus position in increments of 0.05 dex (colored circles). Error bars represent one root median square of the distribution of  $g-r$  colors within the bins. There appears to be a significant correlation between dust extinction and locus position.

To assess our method of accounting for dust extinction local to the extragalactic source, we compare these intrinsic  $g-r$  colors to the observed  $g-r$  colors and find that not only are the intrinsic  $g-r$  colors bluer but also that the degree of attenuation is a function of locus position (see Chapter 5). The distribution of colors, as shown in Figure 3.3 (left), is more narrow for the intrinsic  $g-r$  colors than for the observed  $g-r$  colors. We bin the observed and intrinsic  $g-r$  colors with respect to the locus position of their corresponding emission lines in increments of 0.05 dex to compare the two statistically. As shown in Figure 3.3 (right), the difference between fiber and spectral color correlates strongly with locus position as does the dispersion of values with respect to the bin medians.

Our goal in computing the intrinsic  $g-r$  color, ultimately, is to constrain the

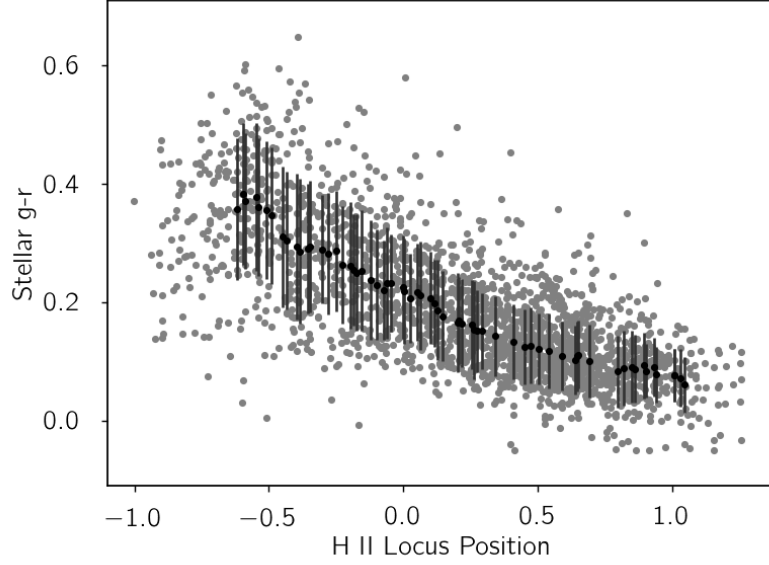


**Figure 3.4:** Locus position versus intrinsic  $g - r$  color for the entire H II sample (grey dots) binned in increments of 0.05 dex with respect to  $[\text{OIII}]/\text{H}\beta$ ,  $[\text{NII}]/\text{H}\alpha$ , and locus position (black dots). Error bars represent the root-mean-square of the  $g - r$  colors in each bin.

locus position of the putative starburst component in the mixing model. To this end, we compare the intrinsic  $g - r$  color to the locus position of the H II region in Figure 3.4 and notice a strong inverse correlation with a Pearson correlation coefficient of  $R = -0.63$ .

Because of the findings of HFS93, we expect, as was the case in purely star forming galaxies, early spectral type stars to dominate the starlight continuum in a true composite galaxy. With this basis, it is reasonable to assume that a true composite's color corresponds directly to OB associations which power the hypothetical nuclear H II regions. Since the intrinsic  $g - r$  color is closely correlated with locus position, the composite's color should correspond to a place in the star forming sequence on the BPT diagnostic diagrams.

For each locus position inferred from the Monte Carlo AGN flux ratios and



those for an observed composite candidate, we can statistically determine the color expected for a composite candidate containing a starburst at this position. Given a locus position solution, we define a circular bin with a radius of 0.154 dex around the predicted locus position in the primary BPT diagnostic (two standard deviations of the starburst sample from the center of the H II locus) and compute the median  $\langle g-r \rangle$  value and root-median-square standard deviation  $\text{rms}_{g-r}$  of the intrinsic  $g-r$  color for galaxies with emission-line flux ratios which fall inside the bin. Then, we compare the composite color  $(g-r)_{\text{obs}}$  to the color characteristic of locus position to assess the probability that the predicted starburst matches the observed stellar population. Quantitatively, we define the the quantity

$$\sigma_{g-r} = \frac{\langle g-r \rangle - (g-r)_{\text{obs}}}{\text{rms}_{g-r}} \quad (3.4)$$

to gauge the significance of the difference between the two observables, i.e., how likely it might be for the composite’s color to fall within the expected distribution of  $g-r$  for the given model parameters.

### 3.2 Constraining AGN Fraction

To establish a baseline of objects characteristic of active galaxies, we select a sample of emission-line galaxies from the Portsmouth analysis (Thomas et al. 2013) of the eighth data release (DR8) of the SDSS (Aihara et al. 2011) using the **GANDALF** code with the stellar population synthesis templates of Maraston and Strömbäck (2011). We require that all objects have well-detected relevant emission lines, which we define as meaning  $A/N > 3$  and less than 33% uncertainty in the flux measured for  $H\beta$ ,  $[\text{OIII}]$ ,  $H\alpha$ ,  $[\text{NII}]$ , and  $[\text{SII}]$ <sup>5</sup>. All objects meeting the

---

<sup>5</sup>While  $[\text{OI}]\lambda 6300$  is an excellent gauge of the partially ionized NLR in AGN (e.g., VO87), the line is often weak or undetected. While including this feature in our empirical correlations

detection requirements are further segregated based on their line ratios; we retain only those objects falling above the  $[\text{NII}]/\text{H}\alpha$  and  $[\text{SII}]/\text{H}\alpha$  maximum starburst lines from Ke01. This gives us a sample of 9475 “pure” active galaxies<sup>6</sup> to use as a baseline comparison sample, larger than the distance-limited AGN sample of Moran et al. (2014) by a factor of  $\sim 10$ .

In the primary BPT diagnostic diagram, which we show in Figure 3.5 (left), the AGN “branch” is nearly perpendicular to the Ke01 demarcation. Figure 3.5 (left) also demonstrates a gradient in the  $[\text{SII}]/\text{H}\alpha$  flux ratios across the AGN branch from  $-0.6$  to  $0.1$  in logarithmic space, a range of nearly a factor of five. This gradient is aligned with the Ke01 line and appears relatively invariant with distance from that demarcation. This gradient might not come as a surprise: both the  $[\text{NII}]/\text{H}\alpha$  and  $[\text{SII}]/\text{H}\alpha$  line ratios gauge the extent of a partially ionized region ranging from the neutral helium Strömgren radius to the hydrogen Strömgren radius because these two species have ionization energies similar to those of neutral hydrogen and neutral helium (Osterbrock and Ferland 2006, henceforth OF06). While the nitrogen emission lines relative to hydrogen tend to be more sensitive to variations in metallicity due to stellar manufactory processes than those of sulfur (e.g., Ka03, Ke06, Nicholls et al. 2017), the  $[\text{NII}]/\text{H}\alpha$  and  $[\text{SII}]/\text{H}\alpha$  line ratios still correlate with  $R = 0.634$ , in all likelihood a result of the similar ionization potentials between the two species.

What makes this map of  $[\text{SII}]/\text{H}\alpha$  across the  $[\text{NII}]/\text{H}\alpha$  BPT diagnostic diagram particularly useful for constraining the AGN fraction, however, lies in determining

---

would greatly improve our potential constraints on composite model results, the requirement that this line be detected at  $\text{A/N} > 3$  reduces the size of the baseline by a factor  $> 2.5$ , limiting the large-number statistics we need in order to characterize this group of objects.

<sup>6</sup>These are not necessarily uncontaminated by a star-forming component; rather, this is a class of objects which cannot be described or modeled as nebulae solely powered by OB associations (e.g., Cid Fernandes et al. 2010). Thus, these objects are not necessarily “pure” but instead must contain a non-starburst component.

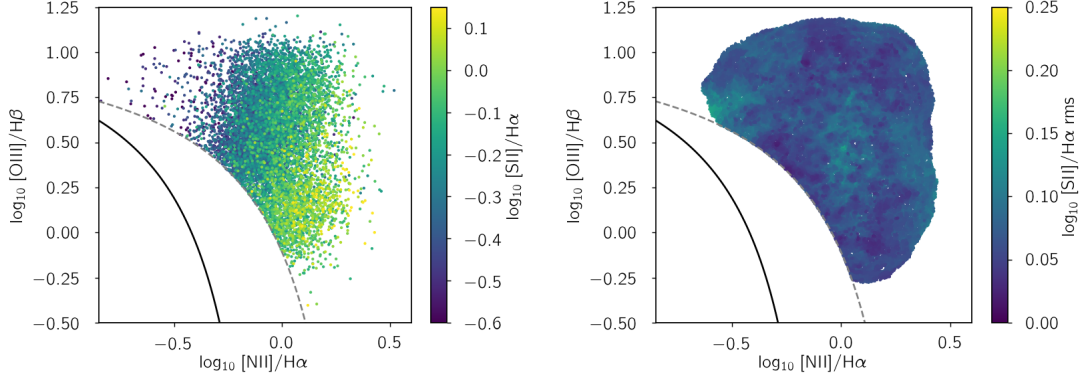


**Figure 3.5:** *Left:* Primary BPT diagnostic showing the AGN sample color-coded according to  $[\text{SII}]/\text{H}\alpha$ . *Right:*  $5 \times 10^4$  Monte Carlo AGN flux ratios sampled from the primary BPT diagnostic (dots). Each pair of flux ratios is color-coded by the root-mean-square of the  $[\text{SII}]/\text{H}\alpha$  flux ratios which fall within the bin aperture centered on each AGN point.

the implied  $[\text{SII}]/\text{H}\alpha$  flux ratios for the Monte Carlo AGN. To do so, we return to the formalism discussed in Chapter 2. From Equation 2.10, we solve the composite mixing model for the  $[\text{SII}]/\text{H}\alpha$  flux ratios, which allows us to determine the AGN contribution from the H II locus position, AGN fraction, and observed line ratios such that

$$\frac{[\text{SII}]}{\text{H}\alpha}_{\text{AGN}} = \frac{[\text{SII}]}{\text{H}\alpha}_{\text{SF}} - \frac{1}{f_{\text{AGN}}^{\alpha}} \left( \frac{[\text{SII}]}{\text{H}\alpha}_{\text{SF}} - \frac{[\text{SII}]}{\text{H}\alpha} \right), \quad (3.5)$$

where  $[\text{SII}]/\text{H}\alpha_{\text{SF}}$  is given by the predicted  $[\text{OIII}]/\text{H}\beta$  value for the  $[\text{NII}]/\text{H}\alpha$  locus position and the fit to the  $[\text{SII}]/\text{H}\alpha$  star forming locus. With this ability to predict additional line ratios, we can produce  $[\text{SII}]/\text{H}\alpha$  line ratios for each Monte Carlo AGN that would be characteristic of the AGN contribution to the composite galaxy given the AGN fraction and starburst components. This provides a useful constraint: because  $[\text{NII}]/\text{H}\alpha$  and  $[\text{SII}]/\text{H}\alpha$  are correlated for objects above the maximum starburst demarcations, a comparison of the  $[\text{SII}]/\text{H}\alpha$  inferred from Equation 3.5 to the  $[\text{SII}]/\text{H}\alpha$  expected for the Monte Carlo AGN will demonstrate the probability that the computed AGN fraction is a viable solution to the mixing

hypothesis.

As was done with the locus position, we draw a bin in the  $[\text{NII}]/\text{H}\alpha$  diagnostic centered on the Monte Carlo AGN line ratio and with a radius of 0.05 dex. However, unlike the tightly distributed H II galaxies along the star-forming locus, the points are spread out. This results in some bins enclosing few to no comparison galaxies. If this occurs, the bin radius is extended iteratively by factors of  $\sqrt{2}$  until at least 5 galaxies are culled for statistics or a maximum radius of 0.283 dex is reached. If the bin contains less than five galaxies when its radius reaches this value, we discard the line ratios preemptively on grounds that such a solution is unlikely. Figure 3.5 (right) shows the retained flux ratios from one such Monte Carlo sampling after binning and rejection, colored according to the root-mean-square  $[\text{SII}]/\text{H}\alpha$  ( $\text{rms}_{[\text{SII}]/\text{H}\alpha}$ ) of galaxies within the bin aperture drawn about each pair of flux ratios. What is particularly significant about the dispersion of  $[\text{SII}]/\text{H}\alpha$  across the sampling bins is that the  $\text{rms}_{[\text{SII}]/\text{H}\alpha}$  is small and relatively invariant: the median rms is 0.071 dex with a 0.012 dex standard deviation. Following from Equation 3.4, we define the agreement  $\sigma_{[\text{SII}]/\text{H}\alpha}$  between the baseline and predicted flux ratio such that

$$\sigma_{[\text{SII}]/\text{H}\alpha} = \frac{\langle [\text{SII}]/\text{H}\alpha \rangle - ([\text{SII}]/\text{H}\alpha)_{\text{brc}}}{\text{rms}_{[\text{SII}]/\text{H}\alpha}} \quad (3.6)$$

where  $\langle [\text{SII}]/\text{H}\alpha \rangle$  is the bin median and  $([\text{SII}]/\text{H}\alpha)_{\text{brc}}$  is the flux ratio projected by the model using Equation 3.5.

### 3.3 Demonstration of Method

How do these empirical correlations and comparisons constrain the simple mixing model predictions computed in Chapter 2? The culmination of these

different components is best shown in practice in order to highlight each aspect. We select what we consider to be a prototypical composite galaxy, J1351+4012, from the Moran et al. (2014) sample as a demonstration of the implementation of our technique and empirical interpretation of its results. We simulate 25000 pairs of flux ratios in the primary BPT diagnostic diagram using the uniform random number generator `rand` in the `numpy.random` module. Using a root-finding routine, we infer AGN fractions, locus positions, and  $[\text{SII}]/\text{H}\alpha$  flux ratios for all Monte Carlo flux ratio pairs. After eliminating solutions where  $f_{\text{AGN}} < 0$  or  $f_{\text{AGN}} > 1$ , we are left with  $23900 \times 10^4$  viable AGN flux ratios.

For all these model solutions, we compare the composite  $g - r$  color to each  $g - r$  color implied by the inferred locus positions to compute  $\sigma_{g-r}$ . We also compute  $\sigma_{[\text{SII}]/\text{H}\alpha}$  for each solution using the inferred AGN  $[\text{SII}]/\text{H}\alpha$ . To assess the net empirical feasibility of each of the mixing model solutions, we add the two statistics in quadrature for a total agreement  $\sigma_{\text{tot}}$

$$\sigma_{\text{tot}}^2 = \sigma_{g-r}^2 + \sigma_{[\text{SII}]/\text{H}\alpha}^2. \quad (3.7)$$

We compute  $\sigma_{\text{tot}}$  for every set of model solutions in our Monte Carlo simulation which gives physically real values for  $f_{\text{AGN}}$  and has enough corresponding baseline galaxies to obtain statistically sound empirical constraints. If an observed composite-classed object has solutions with  $\sigma_{\text{tot}} < 1$ , the object can be considered truly composite galaxy. On the other hand, we suggest composite-classed objects having no solutions with  $\sigma_{\text{tot}} < 5$  fail our hypothesis and are therefore not composites. Ambiguous results, i.e., those where  $1 < \sigma_{\text{tot}} < 5$ , bear closer inspection before making any final assessment. However, if a reasonable fraction, say at least 1%, of the total set of solutions have  $\sigma_{\text{tot}} < 1$ , it is reasonable to consider the

object a true composite.

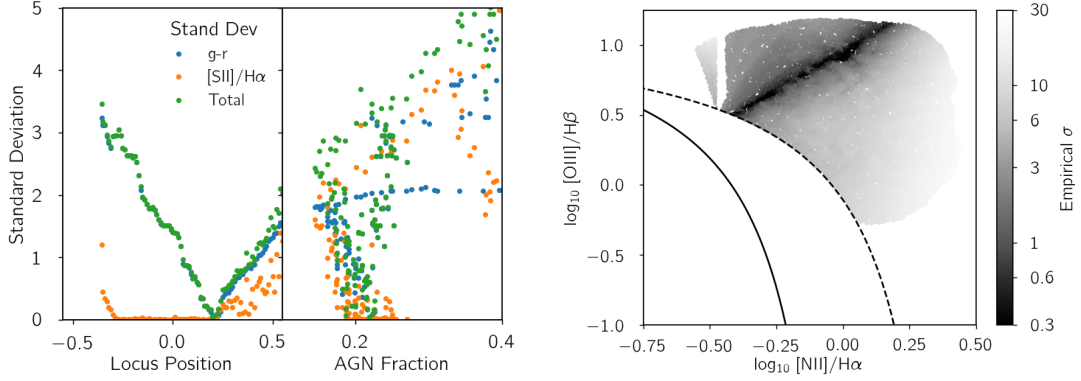


**Figure 3.6:** *Left:* Empirical restrictions on permitted values of locus position and AGN fraction. *Right:* Monte Carlo flux ratios for AGN, color-coded by  $\sigma_{tot}$  for their inferred parameters to highlight which are most likely. Note the distinct dark stripe in the solution set which ranges from the Ke01 demarcation up and to the right across the diagram.

The constraints of  $\sigma_{g-r}$ ,  $\sigma_{[SII]/H\alpha}$ , and  $\sigma_{tot}$  on locus position and AGN fraction for J1351+4012 are shown in Figure 3.6 (left) as well as the reduced permitted region for AGN flux ratios which satisfy the mixing hypothesis for the observed composite (right). There is still a swath of possible solutions across the diagnostic diagram, which appear in the  $\sigma_{tot}$ -colored plot in Figure 3.6 as a narrow locus of solutions arching from the Ke01 demarcation up and to the right across the entire region occupied by AGN flux ratios. We take this tight constraint to indicate the object is truly composite; however, it is unclear at this time which of these solutions is most characteristic of the AGN component.

Lacking additional insight at this time, we weight the assumed AGN flux ratios, AGN fraction, and starburst locus results according to  $\sigma_{tot}$  in order to obtain the expected value for the assumed and inferred parameters such that, for some set of values  $X$ ,

$$\langle X \rangle = \frac{\sum_i X_i \exp(-0.5\sigma_{tot,i}^2)}{\sum_i \exp(-0.5\sigma_{tot,i}^2)} \quad (3.8)$$

gives the characteristic parameter for the mixing model solution. We apply this to both inferred parameters and both assumed flux ratios to obtain quantities which are characteristic of the composite. Using Equations 2.11 and 2.12, we construct a hypothetical mixing sequence based on the weighted-mean locus position and Monte Carlo flux ratios over the full range of possible AGN fractions (Figure 3.7). While the mixing sequence passes directly through the composite flux ratios at the AGN fraction implied for the composite, this was not a requirement imposed on this final mixing sequence because it was constructed solely from weighted-mean parameters. In its own right, this is perhaps a compelling result; however, it is necessary to confirm the accuracy of our method’s predictions before attempting to use its results for scientific purposes.

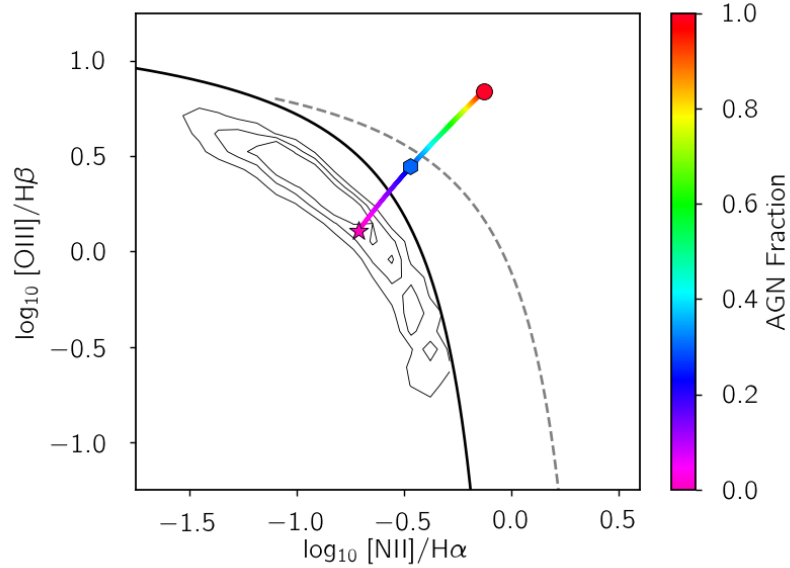


**Figure 3.7:** Mixing sequence solution for J1351+4012 suggested by the  $\sigma_{tot}$ -weighted mean of AGN fraction, locus position, and Monte Carlo flux ratios. Symbols and colors as in Figure 2.1.

## Chapter 4

### The Purpose Breaks

---

And what you thought you came for  
Is only a shell, a husk of meaning  
From which the purpose breaks only when it is fulfilled  
If at all. Either you had no purpose  
Or the purpose is beyond the end you figured  
And is altered in fulfilment

— “Little Gidding”, T. S. Eliot

---

Here, we confront our decomposition predictions with spatially resolved spectroscopic data in order demonstrate the effectiveness of our method and the success (or failure) of the composite hypothesis for individual objects. First, we examine previous studies of composite galaxies done by R. Davies and collaborators to contextualize our motivations. Then, we construct a sample of objects from Siding Spring Seyfert Spectroscopic Snapshot Survey (S7; Dopita et al. 2015, Thomas et al. 2017; henceforth Do15 and Th17, respectively) final IFU data release. We run our model on synthesized single-aperture spectra for the sample and compare our predictions against the spaxels enclosed by the aperture. While the initial test for compositeness works, we find that not all composite-classed objects are true composites. What’s more, we find that the simple linear combination model is not complete enough to fully describe the observations, which portends a need for a more complex model.



## 4.1 Fruit from the Integral Field

A series of papers by R. Davies and collaborators from 2014-17 have explored in detail the nature of true composites with IFU spectroscopy (Davies et al. 2014a, Davies et al. 2014b, Davies et al. 2016a, Davies et al. 2016b, Davies et al. 2017) using S7 and the Calar Alto Legacy Integral Field spectroscopy Area survey (CALIFA; Sánchez et al. 2012). What they suggest, ultimately, is that

the spectra along those [composite] mixing sequences can be reasonably approximated by linear superpositions of the line luminosities extracted from an H II region basis spectrum and an AGN NLR basis spectrum

where the basis spectra are selected from the minimum and maximum  $\log_{10}[\text{OIII}]/\text{H}\beta$ , respectively (Davies et al. 2016b). They fit the IFU spectral line luminosities with a simple linear sum of the basis spectra luminosities weighted by what they call “superposition coefficients”, which are treated as free parameters for each spaxel and closely resemble our own flux fractions in our mixing model.

In the process of demonstrating this assertion, they uncover several significant characteristics of true composite galaxies. They show that the H II component is confined to one place on the star forming locus of the principle BPT diagnostic. They find in all publications that composite galaxies in their sample (which are primarily barred spirals with  $M_{\star} > 10^{10} \text{ M}_{\odot}$ ) tend to have high chemical abundances with relatively invariant metallicity along the mixing sequence. Looking at a total of nine galaxies, they conclude that mixing sequences are dichotomous, with only one subset exhibiting the proposed continuous linear combination of emission lines. As did Ke06, Davies and her collaborators mention in all five papers that pAGB stars and/or shocks and diffuse gas might also contribute to the mixing sequence, posing as H II galaxies or AGN in the BPT diagnostics. This is

explored more thoroughly in the Davies et al. (2017) paper in application to one galaxy, NGC 613, in the context of shocks triggered by gas flows.

While we have independently defined AGN and star forming fractions in the same way as Davies et al., we make no such assumptions about the basis spectra because we have established a method that does not rely on costly integral field spectroscopy. The Davies collaborations are not predictive about the mixing sequences and only go so far as to conduct photoionization models they consider to be representative of the composite components and assemble hypothetical mixing sequences for various AGN fractions. Because the Davies collaborations have demonstrated so rigorously that IFU data can “dissect” galactic nuclei to reveal various line-emitting components, we turn to this as a possible test for our decomposition method for large single-aperture spectra.

#### 4.1.1 The S7 IFU Data

Following in part from the Davies collaborations, we choose to utilize the publicly available second data release of the S7 (Th17)<sup>1</sup>. In total, it contains observations of 131 galaxies selected from the Véron-Cetty and Véron catalogs with the criteria that the objects be southern (declination  $< 10^\circ$ ) to minimize atmospheric extinction, at least  $20^\circ$  above or below the Galactic plane to minimize Galactic extinction, local ( $z < 0.02$ ) to maximize spatial resolution in the host galaxies, and brighter than 20 mJy in the radio 20 cm band to ensure the presence of nuclear activity (due to the limits of radio surveys, this also largely means declination  $> -40^\circ$ )<sup>2</sup>. Observations were taken using the Wide Field Spectrograph (WiFeS), which covers a  $25'' \times 38''$  field of view with a  $1'' \times 1''$  scale for each spaxel.

<sup>1</sup>Available at <https://miocene.anu.edu.au/S7/>.

<sup>2</sup>We note that the radio detection is not necessarily a sound criterion for assembling a Seyfert sample as star formation can also produce emission at 20 cm in nearby galaxies.

WiFeS uses a double spectrograph with  $R = 3000$  for the blue end, covering  $3500 - 5700 \text{ \AA}$ , and  $R = 7000$  for the red, covering  $5400 - 7000 \text{ \AA}$ .

As described both in Do15 and Th17, the WiFeS data releases consist of data cubes of the reduced, flux-calibrated spectra produced by their software `pyWiFeS`. The S7 DR2 also contains data cubes of results from their spectral fitting code `LaZy IFU` (LZIFU; Ho et al. 2016), which performs continuum subtraction and emission line fitting to recover relevant emission line fluxes with the assistance of a neural network. Also included are their custom  $4''$  apertures centered on the nucleus of each galaxy meant to simulate the large SDSS spectral aperture. To that end, they sum the spectra which fall inside the aperture for each galaxy and fit each resulting “nuclear” spectrum using LZIFU. They include both the “nuclear” spectrum and the aperture from which it was extracted in the data release.

### 4.1.2 Decomposition Test Samples

According to Th17, 34 of the 131 objects (26%) contain both Seyfert and starburst emission signatures. However, we choose to examine solely the simulated single-aperture emission line fluxes to define our sample of composite objects. For this, we utilize both the fluxes obtained from fitting the spectrum summed up from within the aperture and the fluxes obtained from summing the results of fitting each individual spectrum within the aperture. To ensure sound data quality in the composite sample, we also impose that all 13 spaxels in the nuclear aperture have well-detected ( $F_\lambda \sigma_{F_\lambda}^{-1} > 3$ ) fluxes from each of the  $H\beta$ , [OIII],  $H\alpha$ , and [NII] lines.

We require that each object fall at least 0.01 dex below the Ke01 and 0.01

dex above the Ka03 demarcations on the primary BPT diagnostic for both the summed spaxel and nuclear spectrum line ratios. This ensures consistency between the large aperture and spaxel line ratios while also accounting for any error in flux measurement which might result in a different classification<sup>3</sup>. Alone, these requirements produce a sample of 14 composite galaxies. Objects which satisfy the data quality requirement and one, but not two, of our composite criteria are examined by eye to determine if the rejection was spurious given the distribution of their nuclear spaxels in BPT space. After this inspection, we add two more galaxies to our composite sample. Any objects with ambiguous classification according to spaxel flux ratios, i.e., a sequence of putative mixing between star formation and some additional source is evident but lacks flux ratios characteristic in any way of Seyferts (namely galaxies NGC 835 and NGC 1672, which also have contentious literary classifications), are rejected to ensure our proof-of-concept is reliable, which gives a final sample of 12 composite galaxies.

For purposes of verifying our predictions beyond the nuclear aperture, we divide our sample into two subsamples, an “A” group in which each observation contains at least 100 spaxels with well-measured lines and a “B” group which does not. While NGC 4303 originally met the requirements for the A sample, the location of its spaxel line ratios in the primary BPT diagnostic make any detailed classification tenuous at best. For this reason, we have moved it to the B sample. This work focuses on the A sample, leaving the B sample to be discussed in the future. In Table 4.1, we show the final A sample with the classification according to the S7 publications (Do15, Th17) and the NASA/IPAC Extragalactic Database (NED). Figure 4.1 shows  $r$ -band images for the A sample with the S7 aperture

---

<sup>3</sup>Consistency is difficult to maintain as the S7 spectral analysis pipeline often struggles with broad lines and does not always fit the starlight continuum well, which Th17 note in reference to their nuclear spectral fitting but do not comment upon regarding the spaxels in the sample.

drawn in red while Figure 4.2 shows the spectra corresponding thereto.

**Table 4.1:** The A composite sample from the S7.

Object	S7	NED
IC 5169	SB+Sy2	Sy2
MCG -04-49-001	LINER	LINER?
NGC 613	Sy2	Sy?
NGC 4990	SB+Sy2	SB
NGC 6328	SB+Sy2	LINER?
NGC 7714	SB	SB

Because the S7 data release does not include the original stellar templates used to construct the starlight continuum from the observed spectrum, we use their reported values of starlight  $E(B-V)$  for each spaxel to reproduce the multiplicative, wavelength-dependent Calzetti extinction law implemented by **pPXF** to redden the stellar templates during the continuum fitting procedure. We recover the original ssp spectrum by dividing the reported best-fit continuum by this extinction law. This is done for each spaxel in the nuclear aperture. We then sum the original ssp spectra from all spaxels to simulate a single-aperture observation, from which we compute the intrinsic  $g-r$  color using the method outlined in Chapter 3.

## 4.2 Reification

Using the synthesized large-aperture fluxes summed from spaxels, we run our decomposition method to determine the likely AGN fraction and H II locus position parameters. Using these values, we predict the BPT mixing sequences, which we anticipate spaxels will follow from the starburst component to that of the “pure” AGN in the case of true composites. Then, we compare the line ratios of the aperture-enclosed spaxels to the projected mixing sequences to demonstrate how well our method recovers the flux ratios associated with these spaxels. Com-

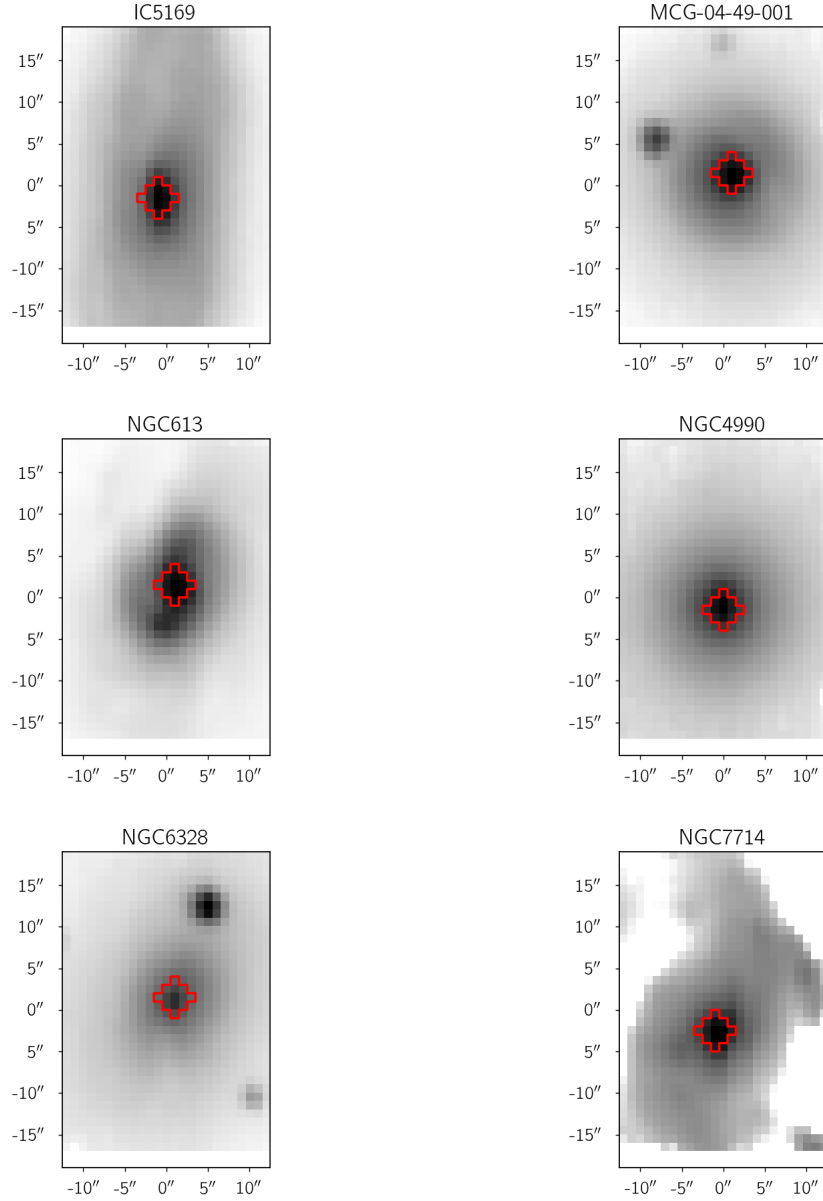


**Figure 4.1:** The location and shape of the S7 "nuclear" aperture for the A sample. Greyscale represents the  $r$ -band AB magnitude of the observed spectrum in each spaxel computed as discussed in Chapter 3. Tick labels are offset from center of observation pointing in arcseconds.

binning the empirical trends and the spaxel line ratio distribution about the mixing sequence, we examine the effectiveness of our technique for decomposing single-aperture spectra of candidate composite objects. Finally, we consider spectral

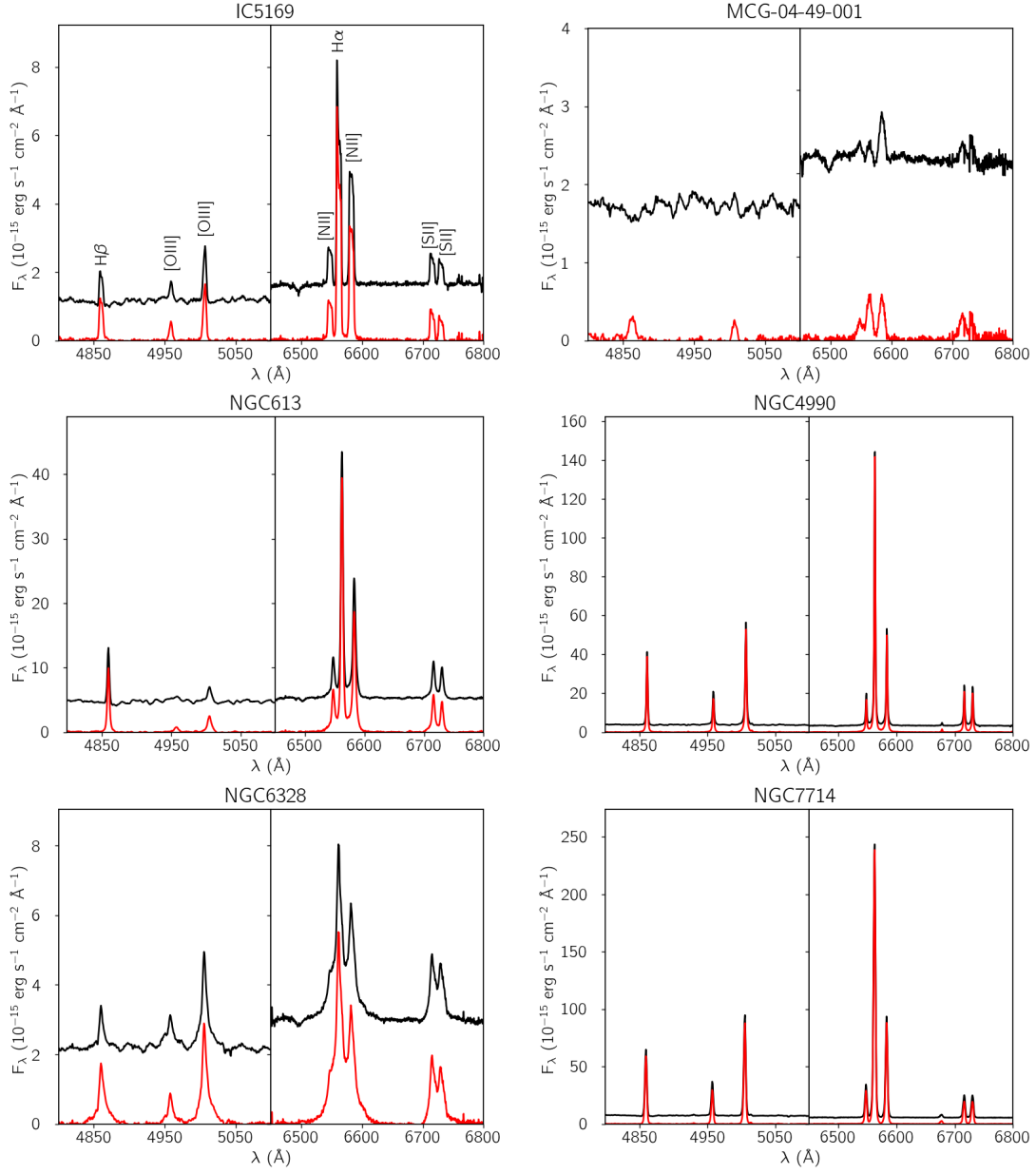


**Figure 4.2:** Strong optical emission lines in the binned nuclear spectra for the A sample. Observed data in black, continuum-subtracted spectrum in red. Relevant emission lines identified in the upper left plot.

information outside the nuclear aperture to investigate whether our predictions drawn from the nuclear spectra are consistent with the full set of spectroscopic data.

### 4.2.1 Decomposition Predictions

With the composite line ratios and stellar population color in hand, we run our model for each object in the A sample with a characteristic Monte Carlo sampling of  $10^4$  possible AGN. We bin the parameters for all solutions with respect to the predicted H II locus position to show the most probable locus position and AGN fraction for each bin, i.e., the parameters with the lowest  $\sigma_{tot}$  (see Figure 4.3 and Table 4.2). There is one very clear success in the A sample, NGC 613, with a large number of solutions closely following the empirical trends in both  $g - r$  and  $[\text{SII}]/\text{H}\alpha$  (i.e., most values of  $\sigma_{tot} < 1$ ) with a strong preference for a particular locus position and AGN fraction (see Figure 4.3). NGC 7714 fails the  $[\text{SII}]/\text{H}\alpha$  test ( $\sigma_{[\text{SII}]/\text{H}\alpha} > 5$ ), apparently ruling out contributions from an AGN. The four remaining galaxies are somewhat ambiguous, however, since all of the constraints have some values of  $\sigma_{tot}$  which fall below the established cutoff for failures but exhibit neither exclusively  $\sigma_{tot} > 5$  nor compellingly low  $\sigma_{tot}$ .

To demonstrate the AGN flux ratios which are fully consistent with the composite hypothesis, we plot in Figure 4.4 the successful Monte Carlo-simulated AGN line ratios in the primary BPT diagnostic with color-coding according to  $\sigma_{tot}$  computed as defined in Chapter 3. The success suggested by the  $\sigma$  vs parameter plot for NGC 613 in Figure 4.3 is notably different from the rest not only because it has lower values of  $\sigma_{tot}$  but also because the simulated AGN with the lowest  $\sigma_{tot}$  form a distinct, narrow stripe as was the case for the archetype J1351+4012 in Figure 3.6. The dearth of viable flux ratios for NGC 7714 continues to suggest no AGN contribution to the emission line flux. The lack of striation, or indeed of any localization, of  $\sigma_{tot}$  in the simulated flux ratios for the remaining objects continues to render the plausibility of compositeness ambiguous. These assess-



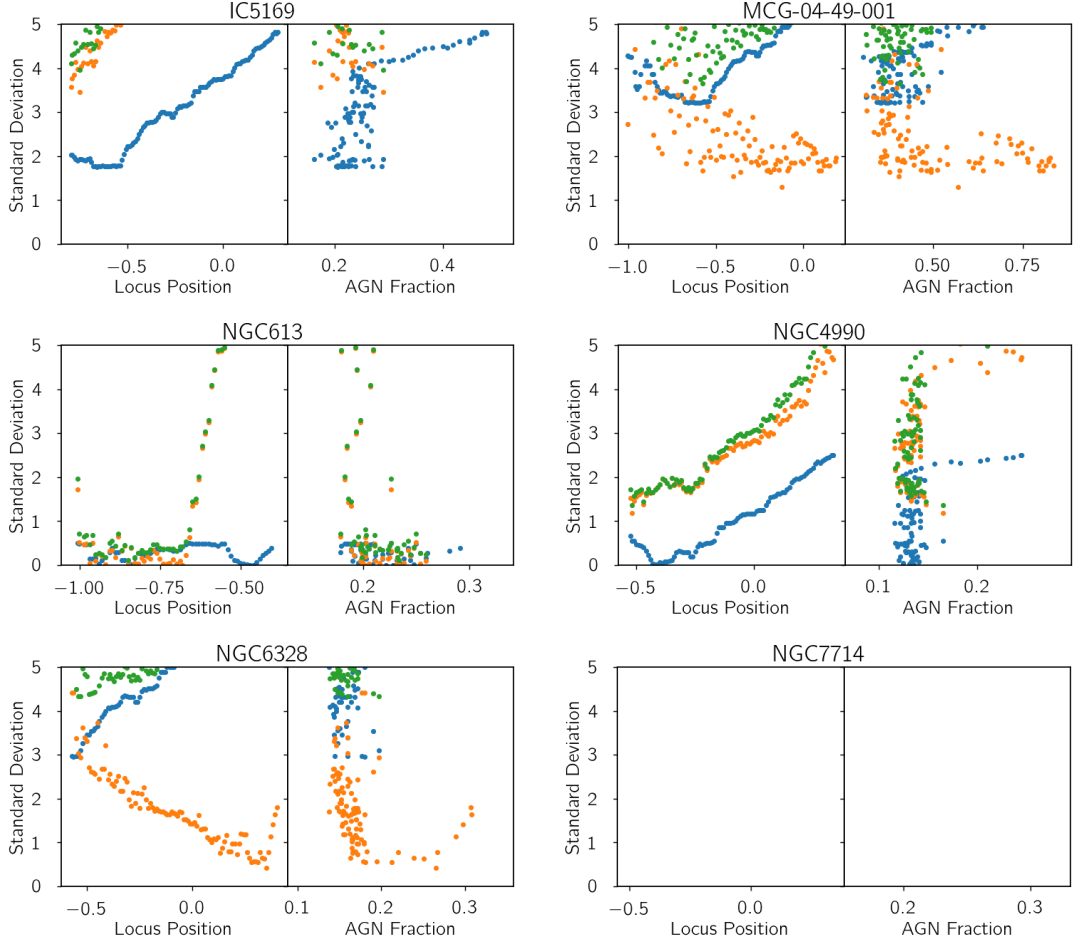


**Figure 4.3:** Empirical constraints on the locus position and AGN fraction parameters of our decomposition method for the A sample. As labeled in the upper left, blue represents the offset of the composite’s  $g - r$  color from that of the predicted H II component, orange the offset of the predicted AGN  $[\text{SII}]/\text{H}\alpha$  from that of the AGN sampled from the Monte Carlo simulation, and green the sum of the two in quadrature.

ments are listed in Table 4.2 under the “Composite Predicted?” headings, which denotes whether our decomposition method has soundly demonstrated or rejected the composite hypothesis for each object in the A sample, independent of the IFU data.

The original aim of turning to IFU data was to assess the accuracy of the mixing sequence predicted by our decomposition method. If the mixing sequence

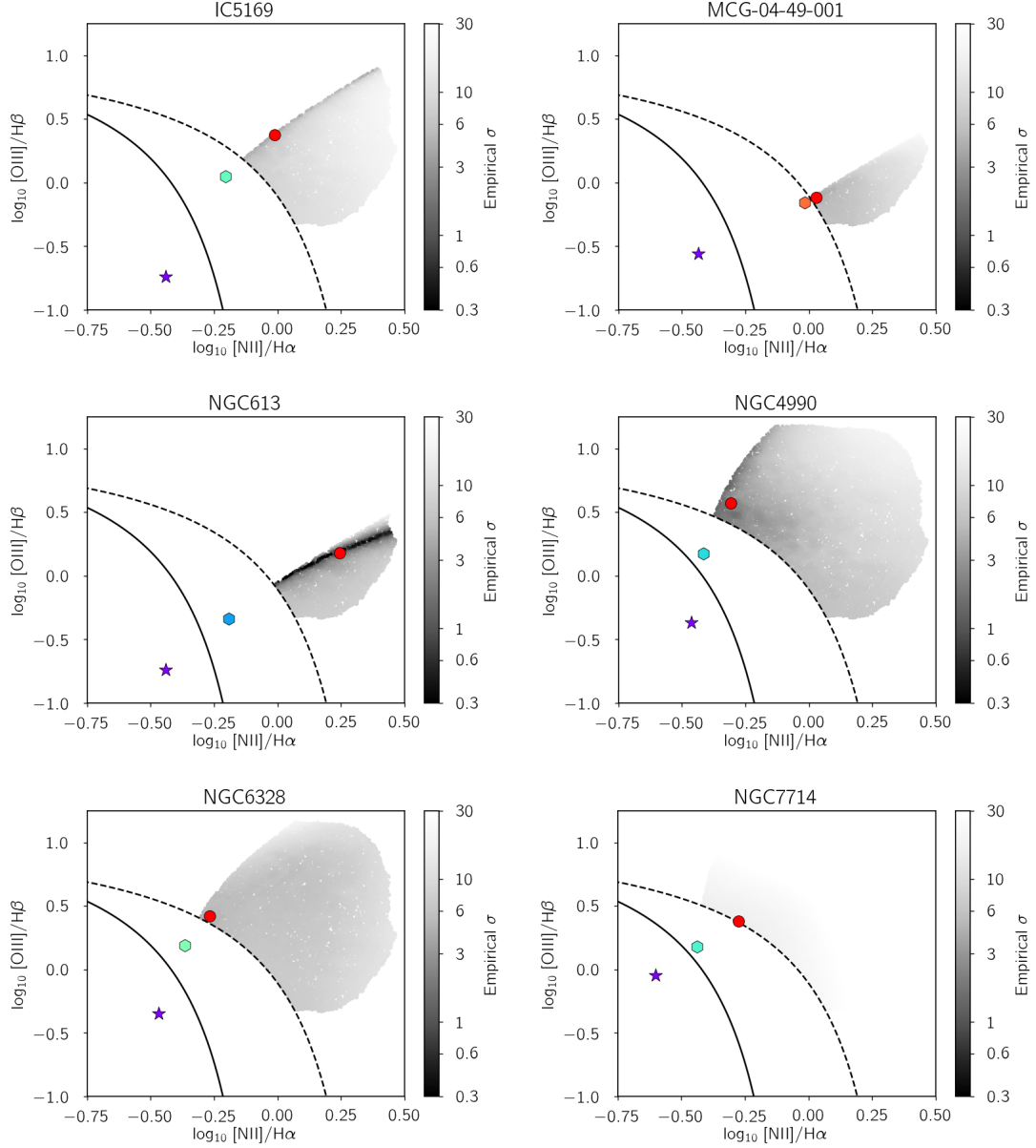


**Figure 4.4:** Empirical constraints on the predicted AGN component of our composite model for galaxies in the A sample. Symbols as in Figure 3.7.

implied by the expected AGN and starburst components is representative of the flux ratios of the spaxels within the nuclear aperture, then we can consider our method reliable and applicable to single-aperture spectroscopic surveys such as the SDSS. To quantify the accuracy of our method, we compute the root-median-

**Table 4.2:** Decomposition test results for the A composite sample from the S7.

Object	Minimum $\sigma_{tot}$	Median $\sigma_{mix}$	Composite Predicted?
IC 5169	3.964	0.602	?
MCG -04-49-001	3.649	0.348	?
NGC 613	0.108	0.513	Y
NGC 4990	1.357	6.914	?
NGC 6328	4.327	0.953	?
NGC 7714	16.114	3.707	N

square of the distribution of all 13 nuclear spaxels about the predicted mixing sequence. Using the `splprep` function from the `scipy.interpolate` module, we compute the B-spline coefficients for a parametric spline of Equations 2.11 and 2.12 with respect to  $f_{AGN}$  for the expected AGN and starburst components. Then, we implement a root-finding minimization method to determine the value of  $f_{AGN} \in [0, 1]$  which minimizes the Euclidean distance between the flux ratios for each nuclear spaxel and the parametric spline representation of the mixing sequence.

With both the parametric representation and the AGN fraction, we compute the Euclidean distance from the mixing sequence for each spaxel's flux ratios such that

$$d_{mix} = \left[ \left( \frac{[\text{NII}]}{\text{H}\alpha}_{obs} - \frac{[\text{NII}]}{\text{H}\alpha}_{mix} \right)^2 + \left( \frac{[\text{OIII}]}{\text{H}\beta}_{obs} - \frac{[\text{OIII}]}{\text{H}\beta}_{mix} \right)^2 \right]^{1/2}. \quad (4.1)$$

The distribution of  $d_{mix}$  is only meaningful if uncertainty in the flux ratios is appropriately considered. As such, we propagate the flux errors reported in the S7 and define

$$\sigma_{mix}^2 = \frac{d_{mix}^2}{\sigma_{[\text{NII}]/\text{H}\alpha_{obs}}^2 + \sigma_{[\text{OIII}]/\text{H}\beta_{obs}}^2} \quad (4.2)$$

to gauge the number of standard deviations of separation between each pair of flux ratios and the predicted mixing sequence. To demonstrate this visually, the minimum Euclidean distance and flux ratio uncertainties are shown for each spaxel’s flux ratios along the mixing sequence for IC 5169 in Figure 4.5.

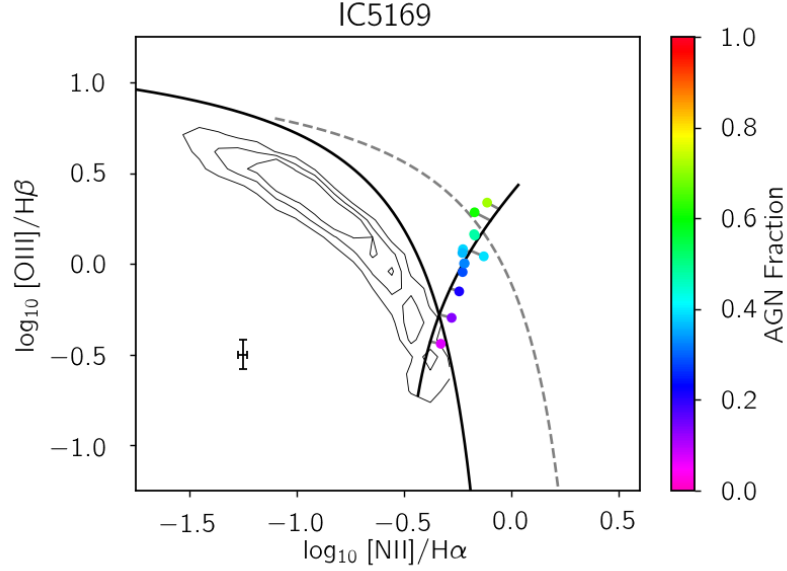


**Figure 4.5:** “Nuclear” spaxel flux ratios (colored circles) distributed about the mixing sequence (dark gray line), colored according to the predicted AGN fraction. Euclidean distances as light gray lines connecting flux ratios and the mixing sequence. Characteristic  $3\sigma$  uncertainty in flux ratios shown in lower left.

We take the square root of the median of  $\sigma_{mix}^2$  to be the characteristic number of standard deviations, which we report for each object in the A sample in Table 4.2. For galaxies NGC 4990 and NGC 7714, the characteristic  $\sigma_{mix}$  demonstrates a disagreement between prediction and observation of more than  $3\sigma$ . In these two cases, we must reject the composite hypothesis as predicted by our method. The rejection of NGC 7714 as a composite is consistent with our minimum computed value of  $\sigma_{tot} = 16.114$ , suggesting our method is a reliable one. However, NGC 4990 has a minimum  $\sigma_{tot} = 1.357$ , suggesting, as the ambiguous model assess-

ments may have implied, that additional empirical constraints may be necessary to improve consistency between model rejection of the composite hypothesis and the IFU data.

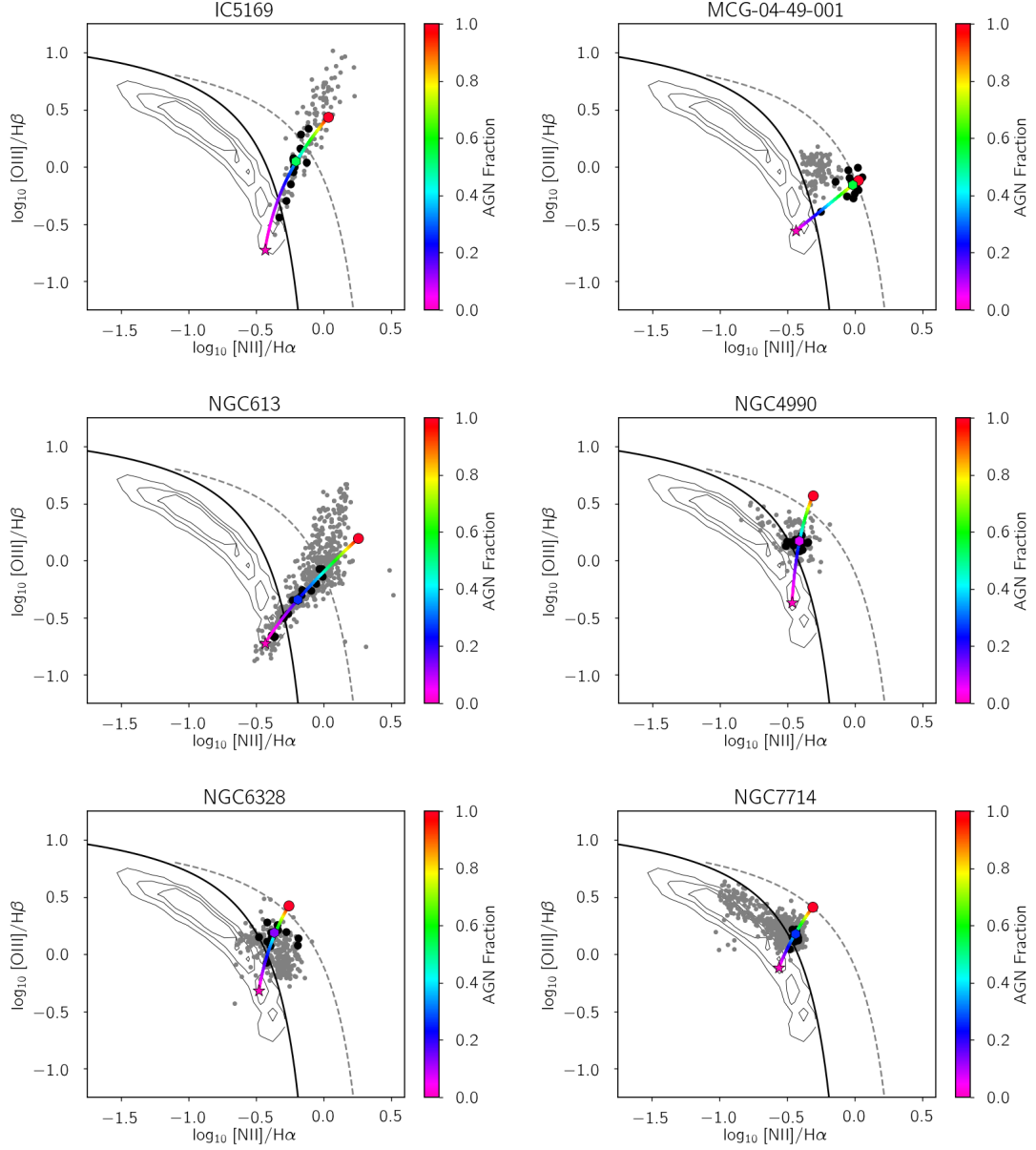


**Figure 4.6:** Mixing model predictions compared to IFU data for the A sample. Predictions represented as in Figures 3.7 and 4.4. Aperture spaxels' flux ratios shown by filled black circles while all spaxels' flux ratios by grey dots.

### 4.2.2 Beyond the Aperture

While part of our stated goal has been to decompose single-aperture nuclear spectra, our motivation is to determine whether an active MBH exists in a supposedly composite galaxy. Some AGN, such as notable Seyfert galaxy NGC 1068 (Heckman et al. 1983) and (perhaps most famous for this trait) NGC 5252 (Unger et al. 1987, Tadhunter and Tsvetanov 1989) have extended NLR (ENLR) far beyond the central kiloparsec of the host, even out to tens of kiloparsecs (e.g., Wilson and Heckman 1985, Wilson, Baldwin, and Ulvestad 1985, Unger et al. 1987, Acosta-Pulido et al. 1990). These results provided the initial science goal of the S7: to explore the physics of ENLRs (Do15). If our positive predictions of the presence of a black hole in these composites are correct, it stands to reason that we might expect to see further spectroscopic signatures of Seyfert activity in the IFU data beyond the nuclear aperture. Inversely, we would not expect to see any trace of MBH accretion in the IFU spectra for our negative predictions, which has potential to be a powerful consistency test. We might also naïvely anticipate the predicted mixing sequences to accurately recover those circum-nuclear spaxels which fall outside the aperture.

In Figure 4.6, we compare our predicted mixing sequences to the line ratios of all S7 spaxels with well-detected emission lines for each object in the A sample. Most simply, the strong failure, NGC 7714, does not agree with the mixing sequence either inside the aperture or out and contains no Seyfert component. This is exactly as anticipated given the strong disagreement between the mixing solutions and empirical correlations. While its  $\sigma_{tot}$  left an ambiguous prediction, IC 5169’s spaxel flux ratios ultimately follow the predicted mixing sequence but extend beyond the predicted AGN point in both  $[\text{NII}]/\text{H}\alpha$  and  $[\text{OIII}]/\text{H}\beta$ . Despite

---

its ability to well reproduce the enclosed nuclear spaxels and indeed a majority of the IFU observation, the most successful composite AGN prediction, that of NGC 613, falls nearly 0.5 dex lower in  $[\text{OIII}]/\text{H}\beta$  than the most Seyfert-like line ratios. To understand the relationship between our predictions and the S7 IFU data in greater detail, we must turn to photoionization modeling.

## Chapter 5

### Intricate Ropes

---

Now I shall ornament you.  
What would you like?  
Baroque scrolls on your ankles?  
A silver navel?  
I am the universal weaver:  
I have eight fingers.  
I complicate you;  
I surround you with intricate ropes  
What web shall I wrap you in?  
Gradually, I pin you down.  
What equation shall  
I carve into your skull?  
What size will I make you?  
Where should I put your eyes?

— “Speeches for Dr. Frankenstein”,  
Margaret Atwood

---

It is essential to ground modeling in rigorous empiricism. While theory can predict upper and lower limits to what we may expect from photoionized nebulae, it is best to inform parameter choices with statistically significant expected values from large numbers of observations of nebulae so that photoionization models can be as accurate as possible. We begin by establishing an H II baseline from the star-forming galaxy sample covered in Chapter 3, using published values to



establish empirical corrections so that the parameter space may be as complete as possible. We then use this baseline to correct the AGN sample for observational bias in order to determine the best state variable selection for the NLR models. We compute oxygen abundances and dust-to-gas ratios to determine the metallicity and dust-depletions in the models. Finally, we select an ionizing continuum which best represents a characteristic accreting MBH.

## 5.1 Published Values

We assemble a set of 789 extragalactic H II regions from various sources in the literature to establish important correlations (see Table 5.1). These include the BPT emission-line fluxes, the [OIII] electron temperature, and relative doubly ionized oxygen and total oxygen abundances,  $[\text{O}^{2+}/\text{H}]+12$  and  $[\text{O}/\text{H}]+12$ , respectively. Because the temperature diagnostic line [OIII] $\lambda 4363$  is difficult to detect (e.g., OF06, Kewley and Ellison 2008), we seek an empirical method for inferring the electron temperature from correlations with readily observed strong emission lines<sup>1</sup>. Additionally, the SDSS spectral coverage stops at 3800 Å, which for low-redshift galaxies like the ones in our sample (recall  $z < 0.0177$ ) excludes the [OII] $\lambda\lambda 3726, 3729$  doublet necessary for completing abundance measurements within the two-zone nebula model (Stasińska 1980). To account for this missing feature, we use the published strong line fluxes to determine a correlation that allow us to correct for oxygen in other ion species.

For the purpose of inferring electron temperatures from prominent emission line ratios, we compare the published electron temperatures to their corresponding H II locus position because, as suggested by Kewley et al. (2013) and implied by

---

<sup>1</sup>It should be noted that the measured electron temperature is not always indicative of the typical temperature of the nebula especially at higher metallicities (e.g., Stasińska 2005), but there is no other readily available empirical diagnostic with which to correct for this.

the Pettini and Pagel (2004) abundance diagnostic, we anticipate that the latter will correspond to evolution in chemical abundance and, thus, changes in electron temperature (e.g., Binnett et al. 2012, Nicholls et al. 2014). An additional motivation for use of the locus position is that, inherent to the VO87 edition of the BPT diagnostics, the line ratios used are insensitive to extinction effects. We find that the correlation between locus position and electron temperature is well described by the hyperbolic function

$$T_4 = \frac{1.822}{\ell + 1.548} - 1.391 \quad (5.1)$$

where  $T_4 = T_e/10^4$  K and  $\ell$  is the locus position, which we show in Figure 5.1 (left).

Additionally, we need to account for the amount of oxygen that exists outside the  $O^{2+}$  species by means of an ionization correction. We approximate the degree of ionization of the gas cloud by examining the line ratio  $[OIII]\lambda 5007$  to  $[OI]\lambda 6300$  because the corresponding ionization potentials are dramatically different ( $O^0$  at 13.6 eV and  $O^{2+}$  at 54.9 eV) and the line ratio is inherently independent of abundance. We demonstrate an empirical relation between the fraction of oxygen which exists in species other than  $O^{2+}$  and the abundance-insensitive line ratio  $\log_{10}[OIII]/[OI]$ , which serves as an ersatz ionization correction factor (in log space, this is just additive) to account for the relative abundance of  $O^+$ . A pair of simple linear regressions gives

$$[O/H] - [O^{2+}/H] = \begin{cases} -0.395 \log_{10} \left( \frac{[OIII]}{[OI]} \right) + 0.994 & , \log_{10} \left( \frac{[OIII]}{[OI]} \right) < 2.3 \\ -0.086 \log_{10} \left( \frac{[OIII]}{[OI]} \right) + 0.282 & , \log_{10} \left( \frac{[OIII]}{[OI]} \right) \geq 2.3 \end{cases} \quad (5.2)$$

which we show in Figure 5.1 (right). Single polynomials with orders ranging from 2 to 7 were also fit to the data; however, these neither properly extrapolated the correlation nor accurately described it.

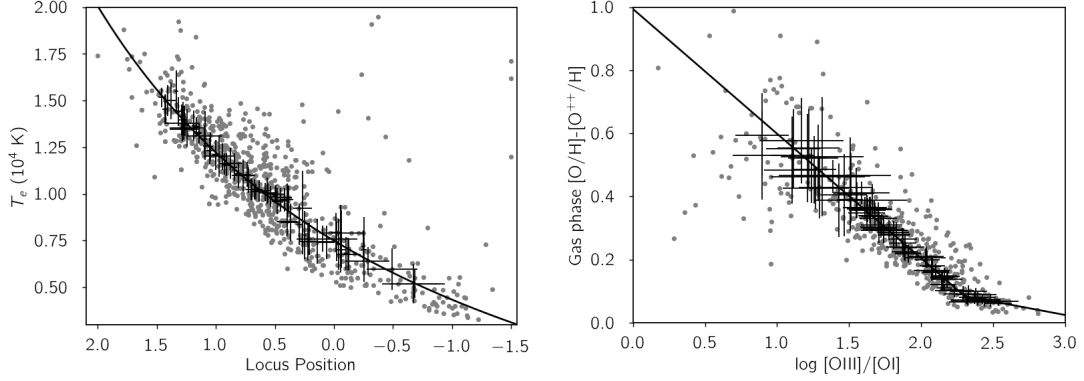


**Figure 5.1:** Empirical correlations from the literature, binned with respect to locus position,  $[\text{OIII}]/\text{H}\beta$ , and  $[\text{NII}]/\text{H}\alpha$ . Error bars represent one root-mean-square of the values in each bin. *Left:*  $[\text{OIII}]$  electron temperature versus locus position. *Right:* Ionization correction factor versus the  $[\text{OIII}]/[\text{OI}]$  line ratio.

## 5.2 Electron Density

The three-level atom model is fundamental to determining the density of the electron gas present in the moderately ionized regions of a nebula. Historically, astronomers have used the  $[\text{OII}]$  doublet in conjunction with this atomic model because the doublet is particularly prominent in nebular spectra. Lacking the  $[\text{OII}]$  lines, we use the  $[\text{SII}] \lambda\lambda 6717, 6731$  doublet, which is still prominent and well-described by the three-level atom for the two transitions ( $^2\text{D}_{5/2}^0 \rightarrow ^4\text{S}_{3/2}^0$  and  $^2\text{D}_{3/2}^0 \rightarrow ^4\text{S}_{3/2}^0$ , respectively) and sensitive to the  $\sim 10^2 \text{ cm}^{-3}$  electron densities we anticipate in nebulae. Using the values for effective collision strength  $\Upsilon$  (i.e., the upper state's collisional strength  $\Omega$  averaged over the energy distribution of the free electron gas) and Einstein coefficient for spontaneous electronic radiative transition  $A$  taken from OF06, we can approximate  $j_{\lambda 6717}/j_{\lambda 6731}$  in terms of the

**Table 5.1:** Literature from which temperature, emission line flux, and empirical abundance data were obtained.

Source	Total	$\ell^a$	$[\text{OIII}]/[\text{OI}]^b$
van Zee et al. 1998	186	186	82
Castellanos, Díaz, and Terlevich 2002	14	14	14
Bresolin et al. 2005	32	32	29
Isotov et al. 2006	309	307	307
van Zee and Haynes 2006	66	65	21
Díaz et al. 2007	12	12	11
Bresolin et al. 2009	28	28	–
López-Sánchez and Esteban 2009	42	42	36
Berg et al. 2012	52	41	34
Nicholls et al. 2014	16	16	14
Hirschauer et al. 2015	13	11	11
Toribio San Cipriano et al. 2017 <sup>c</sup>	18	18	–

<sup>a</sup> Data used to establish the  $T_4 - \ell$  correlation.

<sup>b</sup> Data used to establish the  $[\text{O}/\text{H}] - [\text{O}^{2+}/\text{H}]$  correlation.

<sup>c</sup> While abundances computed from recombination emission lines are reported, only the those derived from collisional emission lines are used.

physical parameter  $n_e T_e^{-1/2}$  tracing the electron density and temperature in the partially-ionized transition zone such that

$$\frac{j_{\lambda 6717}}{j_{\lambda 6731}} = 1.5 \frac{1 + 7.61 \times 10^{-3} n_e T_e^{-1/2}}{1 + 2.58 \times 10^{-2} n_e T_e^{-1/2}}. \quad (5.3)$$

In practice, as  $\Upsilon$  is a function of  $T_e$ , we cannot directly solve for  $n_e T_e^{-1/2}$  without some initial guess for the electron temperature. To determine the density-temperature ratio from the observed line ratios, we iteratively minimize the difference between the observed and predicted values for the [SII] doublet ratio with imposed limits of  $1 \text{ cm}^{-3}$  and  $10^3 \text{ cm}^{-3}$ , using the electron temperature computed as discussed below to approximate the temperature in the [SII] region of the nebula and the 17-node cubic spline to collision strength data from the CHIANTI 8 database (Dere et al 1997, Del Zanna et al. 2015) as implemented by the MAPPINGS

V code (Sutherland and Dopita 2017). For the H II galaxies, we find a median density-temperature of  $3.00 \text{ cm}^{-3} \text{ K}^{-1/2}$  with a logarithmic root-median-square of 0.18 dex, as shown in Figure 5.2 (left).

Brinchmann, Pettini, and Charlot (2008) found that electron density corresponds directly with locus offset and not at all with locus position. Kewley et al. (2013) explain this finding with theoretical models of various H II loci, demonstrating that objects with higher electron densities will produce line ratios up and to the right of the locus. We compare the derived electron density-temperature ratio to the H II locus and find no correlation between either locus position or locus offset ( $R = 0.007$  and  $0.152$ , respectively), which is in conflict with previous findings<sup>2</sup>.

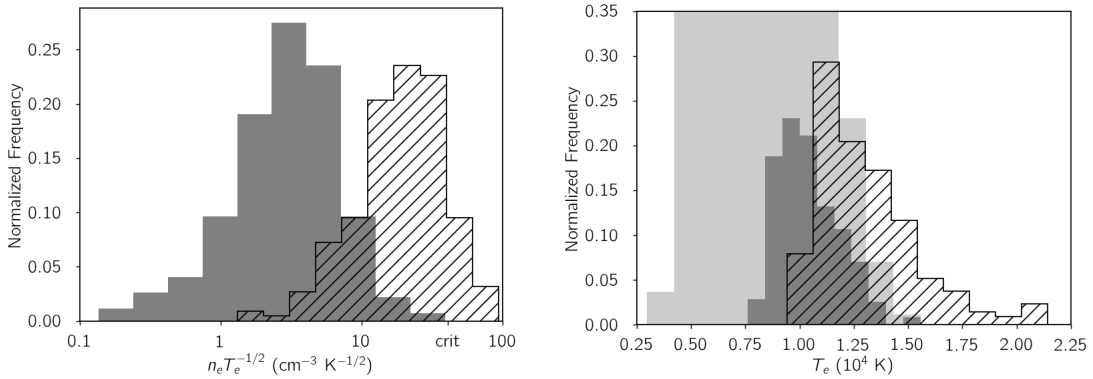


**Figure 5.2:** *Left:* Distributions of electron density-temperature ratios for Seyferts (hashed) and H II galaxies (solid grey). *Right:* As left but for electron temperature. Light grey indicates total H II sample while dark grey highlights directly measured temperatures, demonstrating the detection bias.

For the AGN sample defined in Chapter 3, we compute  $n_e T_e^{-1/2}$  as discussed above and find the density-temperature is  $\sim 0.75$  dex higher than in H II galaxies with a median value of  $19.72 \text{ cm}^{-3} \text{ K}^{-1/2}$  and a 0.22 dex scatter, which we show in

<sup>2</sup>A combination of different parent samples and spectral fitting procedures might account for the discrepancy, as could properly accounting for the electron temperature component of the [SII] ratio.

Figure 5.2 (left). The lower critical density of the two emission lines is also shown in Figure 5.2 (left) to demonstrate the limit at which collisional de-excitations become significant in the partition function of the collisional emissivity. At least 10% of the Sy sample falls above this critical density, which justifies accounting for collisional de-excitations when computing the electron temperature and collisional emissivities.

### 5.3 Electron Temperature

While the [SII] ratio diagnostic relied on the three-level atom model to obtain electron density, the canonical line ratio gauge of electron temperature requires the five-level atom model to describe the [OIII] $\lambda\lambda 4959, 5007$  doublet ( $^1D_2 \rightarrow ^3P_1$  and  $^1D_2 \rightarrow ^3P_2^0$ , respectively) and the auroral [OIII] $\lambda 4363$  ( $^1S_0 \rightarrow ^1D_2$ ). Again using principles and constants from OF06, we derive the approximate relation

$$\frac{j_{\lambda 4959} + j_{\lambda 5007}}{j_{\lambda 4363}} = \frac{7.689 \exp(3.2975 \times 10^4 T_e^{-1})}{1 + 4.371 \times 10^{-4} n_e T_e^{-1/2}} \quad (5.4)$$

which, in a low density case where  $n_e \rightarrow 0$ , can be analytically solved. For the general case, we employ an iterative solution using the density-temperature ratio implied by the [SII] ratio, temperature-sensitive values of  $\Upsilon$ , and a numerical root finding method to minimize the difference between the predicted and observed line ratios<sup>3</sup>. We find that 472 starburst galaxies have detected [OIII] $\lambda 4363$ , meaning only 22% of the sample has directly-measured electron temperatures. For cases

---

<sup>3</sup>This requires we assume, perhaps erroneously, that there exists some consistency in the state variables between the [SII] and [OIII] regions of the nebula. It has been known for some time that the state variables for the electron gas are known to fluctuate spatially depending on the level of ionization in a particular depth of the nebula, to which both density (Osterbrock and Flather 1959) and temperature (Peimbert 1967) are quite sensitive. However, in the absence of additional, more informative data, we are unable to avoid making such assumptions.

where the auroral line is poorly detected ( $A/N < 3$ ) in the H II galaxy sample, we use the  $\ell - T_4$  trend implied by the literature as described above.

Star-forming galaxies with a well-detected auroral line have a median temperature of  $10550 \pm 1100$  K while that of the total H II sample is  $8450 \pm 1500$  K, a difference of 0.1 dex. For the 289 AGN in our sample with well detected auroral [OIII] (a mere 3% detection rate), we compute the electron temperature and find a median of  $12660 \pm 1370$  K. Correcting for detection bias using the 0.1 dex offset gives a characteristic value of 10050 K. Because the auroral line was only detected in Seyferts within the AGN sample, it is reasonable to assert that these values are characteristic of Seyfert NLRs without any inclusion of non-Seyfert LINERs.

## 5.4 Gas Pressure

As has been demonstrated in many studies (e.g., Dopita et al. 2002, Groves et al. 2004a,b), H II regions and the Seyfert NLR are best approximated as an isobaric ideal gas with the equation of state

$$P_e = n_e k_B T_e \quad (5.5)$$

where  $P_e$  is the gas pressure and  $k_B$  the Boltzmann constant. This makes the value  $P_e/k_B$  a significant component for modeling photoionized regions. In order to select appropriate values for  $P_e/k_B$ , we compare values for density and temperature and find they are not correlated ( $R = 0.046$ ). As such, we simply take  $P_e/k_B$  to be the product of  $T_e$  and  $n_e$  in order to find the characteristic  $P_e/k_B$ . In Figure 5.3, we show the logarithmic distribution of  $P_e/k_B$  for our sample of H II galaxies with  $\log_{10} P_e/k_B = 6.38$  with a 0.26 dex root-median-square. We also find the median and rms of  $\log_{10} P_e/k_B$  for galaxies with well-detected auroral [OIII] emission to

determine a correction factor for the median  $P_e/k_B$  of the AGN sample. The H II galaxies with directly measured  $T_e$  have a median  $\log_{10} P_e/k_B = 6.59$  with a 0.18 dex rms, which implies the true characteristic  $P_e/k_B$  is  $\sim 65\%$  less than that implied by the objects with a well-detected auroral line.

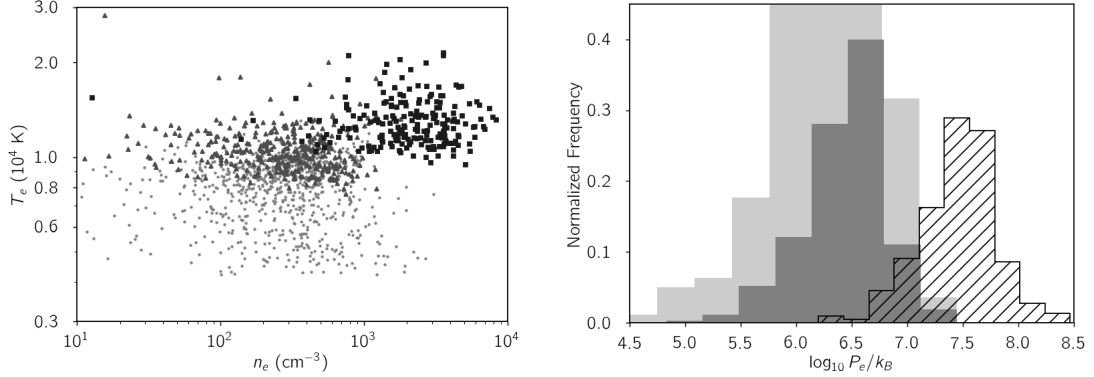


**Figure 5.3:** Empirical values for electron gas state variables. *Left:* The computed electron density and temperature for the star-forming sample and Seyferts with detected auroral [OIII] lines. Black squares represent the Seyferts, dark grey triangles the star-forming galaxies with direct-method electron temperatures, and light grey dots the star-forming galaxies with inferred temperatures (i.e., those objects where A/N for [OIII]  $\lambda 4363$  is  $< 3$ ). Note the detection bias for high temperature H II regions does not favor any particular density. *Right:* Same as temperature distributions in Fig 5.2 but for  $\log_{10} P_e/k_B$ .

For AGN in our sample with well-detected auroral [OIII], we compute  $\log_{10} P_e/k_B$  using the temperatures and densities found above. The median is 7.46 with a 0.21 dex root-median-square. With the 0.1 dex correction, we expect the pressure state variable to be roughly 7.36. Again, these are characteristic of Seyferts as no LINERs had detected [OIII]  $\lambda 4363$  flux.

## 5.5 Chemical Abundance

The flux ratios predicted by AGN photoionization models are strongly dependent on the chemical abundances of the gas in the ISM in the NLR (Groves et al.



2004a,b). As such, it is important for us to model the NLR over a range of chemical abundances with a complete understanding of the impact metallicity might have on other parameters such as the state variables. Because the star-forming and AGN components of a true composite galaxy share a similar chemical evolution history, the chemical abundances are expected to be similar (Evans and Dopita 1987, Storch-Bergman et al. 1998, Ho et al. 2015), so we look to our sample of nuclear H II galaxies to constrain the metallicity we anticipate in the NLR.

To begin, we establish a method for obtaining the approximate relative oxygen abundance  $[\text{O}/\text{H}]+12$ . Then, we demonstrate the abundance cooling sequence with first the literature sample and subsequently with our own sample, providing a method for coupling the initial conditions for the state variables with  $[\text{O}/\text{H}]+12$ . Finally, we discuss the implementation of oxygen-calibrated chemical abundance schemes.

### 5.5.1 Computing Oxygen Abundance

The direct method of determining abundances from collisionally excited lines relies on assuming the emissivity  $j_\lambda$  is

$$j_\lambda = n_{\chi^i} n_e \varepsilon_\lambda(n_e, T_e) \frac{4\pi\lambda}{hc} \quad (5.6)$$

where  $n_{\chi^i}$  is the abundance of a particular element  $\chi$  in ionized species  $i$  and  $\varepsilon_\lambda$  is the emission coefficient (Equation 5.41 in OF06).  $\varepsilon_\lambda$  given by

$$\varepsilon_\lambda = \frac{A}{Z} \frac{k_C \Upsilon}{g T_e^{1/2}} \exp\left(\frac{h\nu}{k_B T_e}\right) \quad (5.7)$$

where  $Z$  is the partition function summing the rates of all transitions out of the current state,  $g$  is the statistical weight of the excited state, and  $k_C = 8.629 \times 10^{-6} \text{ m}^3 \text{ K}^{1/2} \text{ s}^{-1}$  is the collisional constant (Equation 3.20 in OF06). For recombination lines, the assumed relationship from Equation 4.14 in OF06 is

$$j_\lambda = n_{\chi^i} n_e \alpha_{eff} \frac{4\pi\lambda}{hc} \quad (5.8)$$

where  $\alpha_{eff}$  is the effective recombination rate, which accounts for collisions in the transitional cascade which populates the state wherefrom an electronic transition occurs to produce a photon at  $\lambda$ . While OF06 suggest  $\alpha_{H\beta}^{eff} \propto T^{-0.9}$ , Draine (2011) more explicitly defines  $\alpha_{H\beta}^{eff}$  in his Equation 14.9 as

$$\alpha_{H\beta}^{eff} = \alpha_{H\beta,0}^{eff} T_4^{-0.058 \ln T_4 - 0.874} \quad (5.9)$$

where  $\alpha_{H\beta,0}^{eff} = 3.025 \times 10^{-14} \text{ cm}^3 \text{ s}^{-1}$  is the effective recombination coefficient for  $H\beta$  at  $T_e = 10^4 \text{ K}$  and  $n_e = 10^2 \text{ cm}^{-3}$ . Together with the state variables derived above, we can compute  $\varepsilon_\lambda$  for the [OIII]  $\lambda\lambda 4959, 5007$  doublet and  $\alpha_{eff}$  for  $H\beta$  to determine the relative abundance of doubly ionized oxygen,  $[O^{2+}/H]$ , such that

$$\left[ \frac{O^{2+}}{H} \right] = \log_{10} \left( \frac{j_{4959} + j_{5007}}{j_{4861}} \right) - \log_{10} \left( \frac{\varepsilon_{4959} + \varepsilon_{5007}}{\alpha_{4861}} \right). \quad (5.10)$$

To test this method, we apply it to the fluxes and electron temperatures from the literature sample and recover  $[O^{2+}/H]$  within 0.031 dex. With electron temperatures inferred from the BPT H II locus position of the published line fluxes, we recover  $[O^{2+}/H]$  within 0.156 dex with no systemic offset.

Had the [OII]  $\lambda\lambda 3726, 2729$  doublet fallen inside the wavelength range covered by SDSS spectra for local galaxies, we would complete the oxygen measurement

by applying this direct method to those line fluxes to obtain the relative abundance  $[\text{O}^+/\text{H}]$  in keeping with Stazińska’s two-zone nebula model, appropriately scaling the electron temperature to account for variations in the nebular structure (e.g., Isotov et al. 2006). Lacking this, we instead use the ionization correction factor implied for the literature sample above to obtain the total relative oxygen abundance. Our correction-factor technique recovers the total oxygen abundances of the literature within 0.06 dex (0.13 dex with the inferred temperature) of the published values without any systemic offsets<sup>4</sup>.

From the Seyferts with computed electron temperatures, we find those having  $[\text{OII}]\lambda\lambda 3726, 29$  and  $[\text{OI}]\lambda 6300$  fluxes detected with  $A/N > 3$  to compute direct method abundances assuming a three-zone ionization model to account for the extended transition zone such that

$$\frac{\text{O}}{\text{H}} = \frac{\text{O}^0}{\text{H}} + \frac{\text{O}^+}{\text{H}} + \frac{\text{O}^{2+}}{\text{H}} \quad (5.11)$$

with the assumption that the amount of oxygen in the  $\text{O}^{3+}$  ionization state is negligible<sup>5</sup>. While there is substantial bias in this subsample of Seyferts due to the  $[\text{OIII}]\lambda 4363$  detection requirement, we still find that 46% of these Seyferts have supersolar metallicities,  $[\text{O}/\text{H}] + 12 > 8.69$ .

---

<sup>4</sup>This still introduces a consistent sizable systemic error since 0.13 dex represents 35% of the true value. However, lacking the  $[\text{OII}]$  doublet and additional ionization correction factors like  $\text{HeII}\lambda 4686 / \text{HeI}\lambda 5876$  (OF06), this is the best available constraint on the total abundance available to us for our star-forming galaxy sample.

<sup>5</sup>This assumption breaks when the ionizing photon flux of the source exceeds  $\sim 10^{12.5}$  photons  $\text{s}^{-1} \text{ cm}^{-2}$ . According to our preliminary models, the fraction of oxygen locked up in  $\text{O}^{3+}$  increases exponentially to as much as 20% of the total. To account for this, we would need to invoke an ionization correction factor, likely  $j\lambda 4686 / j\lambda 5876$  with the assumption that  $n_{\text{He}^{2+}}/n_{\text{He}^+} \approx n_{\text{O}^{3+}}/n_{\text{O}^{2+}}$ . In light of this, we consider our results to be a lower limit on the true abundance; however, it is relatively rare to find Seyferts which exceed this ionization flux threshold, so any difference between the three- and four-zone model abundances will be small in most cases.

### 5.5.2 Cooling and Evolution Sequences

From the literature and our own sample, we find an immensely strong inverse correlation between  $T_e$  and  $[\text{O}/\text{H}]+12$  ( $R = -0.959$  for H II galaxies) which we describe with the fourth-order polynomials

$$T_4 = 0.021x^4 - 0.568x^3 + 5.471x^2 - 22.051x + 32.843 \quad (5.12)$$

for H II galaxies and

$$T_4 = 0.021x^4 - 0.568x^3 + 5.471x^2 - 22.255x + 35.07 \quad (5.13)$$

for Seyferts, where  $x = [\text{O}/\text{H}]+12$  (see Figure 5.4). Binnette et al. (2012) offer a simple linear regression to explain the correlation given a small number of objects. While Nicholls et al. (2014) provide a simple polynomial fit to describe the cooling sequence for a much larger sample, their relationship only applies to objects with less than solar abundances. Our results in Figure 5.4 extend this work up to metallicities of  $\sim 4$  times solar.

Such a strong correlation suggests a physical mechanism is responsible for the observed relationship. Metals have long been known to act as cooling mechanisms in gaseous nebulae (Spitzer 1949), and a relation between chemical abundance and electron temperature has been demonstrated theoretically (e.g., Stasińska 2005). But it was not until recently that an empirical correlation between the abundances and the electron temperature was established (Binnette et al. 2012). In 2014, Nicholls et al. demonstrated and modeled the correlation between oxygen abundances and electron temperature using photoionization models of H II regions. Because this correlation is due to the loss of kinetic energy in the electron

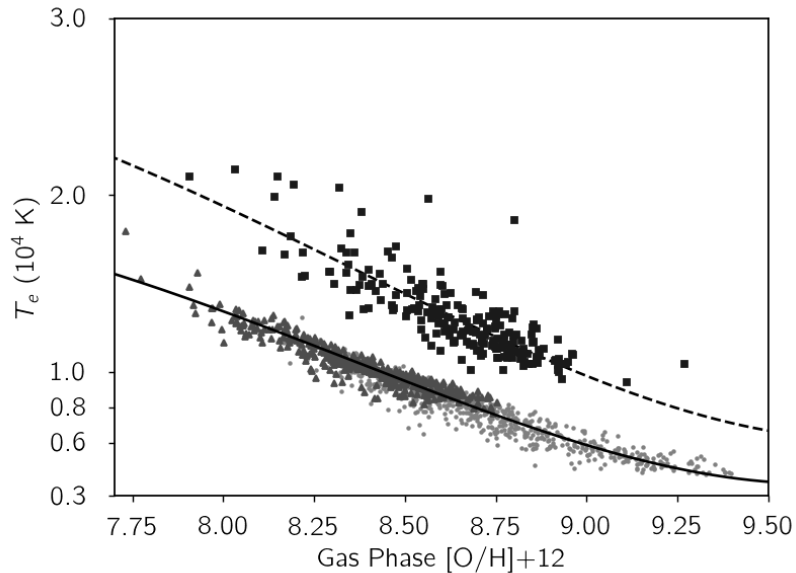


**Figure 5.4:** The abundance cooling sequence as coded in Fig 5.3. Solid and dashed lines are fourth-order polynomial fits to the H II and Seyfert cooling sequences, respectively.

gas through collisions (thereby causing a decrease in the electron temperature), we refer to this correlation as the abundance cooling sequence. We use this abundance cooling sequence to inform our selection of electron temperature for each abundance.

We find that, as suggested by Kewley et al. (2013), the metallicity does indeed vary with respect to locus position (Figure 5.5). We also discover that the intrinsic  $g-r$  color derived in Chapter 3 correlates with metallicity and speculate that the two are coupled as a function of star formation history. Given the trend in Figure 5.5, it stands to reason that the ISM and stellar abundances are related because increased metallicity exacerbates the absorption line blanketing of the stellar spectrum, thereby reddening a stellar population’s intrinsic SED. Indeed, comparisons between stellar and ISM chemical abundances in extragalactic HII regions have found the two are quite similar (e.g., Bresolin et al. 2016).

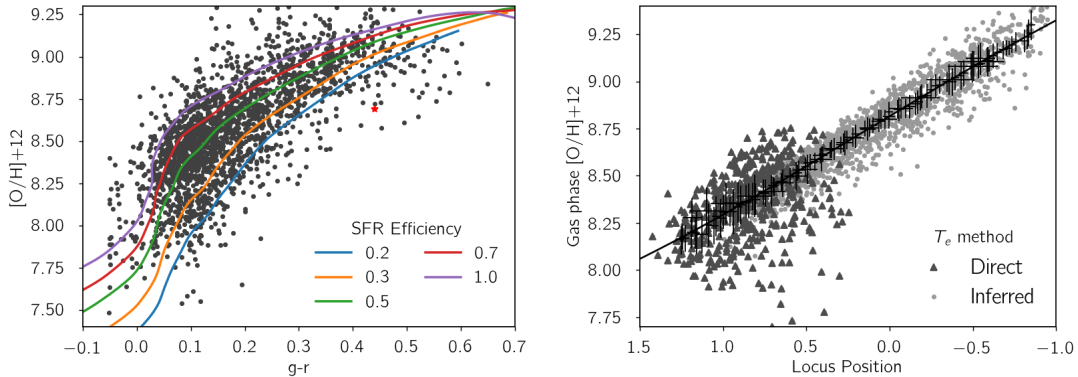


**Figure 5.5:** The evolutionary sequence of star-forming galactic nuclei as shown by (*left*) the color of the associated stellar population and (*right*) the locus position. Lines in left figure are coupled stellar and chemical evolution models for different star formation efficiencies as computed by GALEV.

To explore this idea further, we turn to the GALEV stellar population synthesis code<sup>6</sup> (Kotulla et al. 2009), which couples stellar population synthesis with chemical evolution models to model star formation histories over cosmic time. For a starting epoch of  $z = 10$ , initial baryonic mass of  $10^{10} M_{\odot}$ , and Kroupa IMF, we run GALEV for a range of star formation rate efficiencies<sup>7</sup> and compare the predicted abundances and intrinsic  $g - r$  color values to the observations in Figure 5.5. Given how well the evolution models describe the observed distribution, it is reasonable to consider the correlation of  $[O/H]+12$  with  $g - r$  a demonstration of the coupled evolutions of the ISM and stellar population.

### 5.5.3 Total Abundances

Oxygen is only one element, and, moreover, its abundance is sensitive to element manufactories like the  $\alpha$ -process, the CNO cycle, and Type II supernovae.

<sup>6</sup>See <http://galev.org/>

<sup>7</sup>This efficiency is simply the ratio of star formation rate density to gas density, not to be confused with the efficiency used in the Kennicutt-Schmidt law (Kennicutt 1998) often invoked in star formation models.

As such, we rely on the empirically robust chemical abundance measurements presented in Nicholls et al. (2017) which scale the relative oxygen abundance with other element abundances based on values observed in O and B stars (their so-called Galactic Concordance). Selecting different values in  $[\text{O}/\text{H}]+12$  thus dictates the full abundance set in addition to the state variables. Since we find  $n_e$  is invariant with respect to temperature or abundance, any chosen abundance will indicate the values of  $T_e$  and  $P_e/k$  to use for the isobaric density structure of the model nebula.

## 5.6 Dust

Dust is a significant component of photoionization models (Dopita et al. 2002; Groves et al. 2004a,b) and is necessary to fully explain the observed flux ratios from known AGN. Because dust grains preferentially capture low-velocity electrons, they serve to “heat” the electron gas by reducing the low-energy end of the kinetic energy distribution, thus raising the temperature. To determine the dust content of a nebula, we need to compute the fraction of each total metal abundance that is locked up in the dust grain phase of the interstellar medium (the remainder composes the gas-phase metallicity discussed above). Four decades of research on this “depletion” of metals into the dust phase have led to empirically-constrained dust condensation rates for each metal, all of which scale directly with the iron depletion rate (Jenkins 2013).

We look to constrain this dust depletion rate by determining the dust-to-gas ratio and comparing it to the corresponding metallicity. First, we derive the dust-to-gas ratio using the continuum-fit and intrinsic spectra discussed in Chapter 3 because the stellar population is embedded either within or behind any absorbing medium. Historically, many have used the Balmer decrement to infer the dust-

to-gas ratio; however, the recombination lines originate from extended regions of the nebula and are thus less extinguished than the starlight. It is possible, with assumptions about the Balmer decrement and the scaling of the extended cloud relative to its full depth, to infer the dust-to-gas ratio (c.f., Brinchmann et al. 2013); however, this is prone to bias in assumptions about the temperature-sensitive  $H\alpha/H\beta$  ratio and is unreliable at low metallicities (possibly due to the intrinsic connection between temperature and abundance).

Using the observed and intrinsic starlight continua, the relative dust abundance  $M_{dust}/M_{gas}$  can be approximated from Equation 21.13 in Draine (2011), which is rewritten here as

$$\frac{M_{dust}}{M_{gas}} = \frac{2\rho_{gr}}{3\pi^2\mu_{gas}m_HFN_H} \int_{0.1\mu m}^{2.2\mu m} \tau_\lambda d\lambda \quad (5.14)$$

where  $\rho_{gr} \approx 3 \text{ g cm}^{-3}$  is the characteristic grain mass density for a mixture of graphite and olivine (a realistic assumption, e.g. Mathis, Rumpl, and Nordsieck 1977; Draine 2011),  $\mu_{gas}$  is the mean molecular weight of the gas in its neutral state,  $F \approx 1$  expresses the average geometry of the dust grains (1 being roughly spherical),  $\tau_\lambda$  is the optical depth of the clouds in which the OB association is embedded, and  $N_H$  is the hydrogen column density<sup>8</sup>. The latter most is given by Equation 1 in Güver and Özel (2009) as

$$N_H = 2.21 \times 10^{21} \text{ cm}^{-2} A_V \quad (5.15)$$

where  $A_V$  is the total  $V$ -band extinction in the Johnson-Cousins magnitude system. Because this was obtained using a total-to-selective extinction ratio of 3.1,

<sup>8</sup>An extra factor of 2 appears in the coefficient to account for attenuation in the 2.2-30  $\mu m$  regime which is not well-described by the extinction law and represents roughly half of the dust abundance (Draine 2011). Also note that this ultimately requires conversion from  $\mu m^2$  to  $cm^2$ , meaning there is an unexpressed conversion factor of  $10^8$ .



we correct Equation 5.15 by multiplying by a factor of 4.05/3.1, the numerator being characteristic of the Calzetti extinction law. Combining Equations 5.14 and 5.15 with a general extinction law  $\tau_\lambda = -\ln(I_\lambda/I_{\lambda,0})$ , where  $I_\lambda$  is the intensity of the observed continuum and  $I_{\lambda,0}$  is the intensity of the ssp, gives

$$\frac{M_{dust}}{M_{gas}} \approx \frac{-178.925}{\mu A_V} \int_{0.12\mu m}^{2.2\mu m} \ln \left( \frac{I_\lambda(E(B-V))}{I_{\lambda,0}} \right) d\lambda \quad (5.16)$$

which we apply to the intrinsic and observed continua of our starburst galaxy sample.

We use standard Bessell Johnson-Cousins filter transmission functions to compute  $V$  and  $B$  magnitudes with the method outlined in Chapter 3 from the intrinsic and final subtracted starlight continua and take the differences in each bandpass to obtain  $A_V$  and  $A_B$ , with which we also determine  $E(B-V) = (B_{cont} - V_{cont}) - (B_{intr} - V_{intr})$ . The Calzetti (2001) extinction law allows us to extrapolate  $I_\lambda/I_{\lambda,0}$  beyond the observed SDSS spectrum, which offers a better estimate of the relative dust abundance than the SDSS spectrum alone. Using the composite form of the Simpson's rule method, we compute the integral in Equation 5.16 for each object in the H II sample with  $E(B-V) > 0$ .

Given (a) the relationship between observed and intrinsic  $g-r$  color with respect to the H II locus position shown in Figure 3.3 in Chapter 3 and (b) the  $[O/H]+12$  coupling with locus position shown in Figure 5.5, we anticipate the dust-to-gas ratio to follow closely with the metallicity. We compare the derived dust-to-gas ratios to chemical abundance, which we show in Figure 5.6, and find a relatively strong correlation ( $R = 0.512$ ). This coupling can be explained by the coevolution of dust and chemical enrichment as a function of star formation history

(e.g., Galliano, Dwek, and Chaniai 2008; Popping, Somerville, and Galametz 2017).

To determine the characteristic dust depletion, we compare our dust-metallicity sequence against the range of  $[\text{Fe}/\text{H}]$  dust depletion values from Jenkins (2013) applied to the Nicholls et al. (2017) Galactic Concordance abundances (Figure 5.6). While a range of dust depletions appear to describe the breadth of the distribution here, the  $[\text{Fe}/\text{H}] = -1.25$  abundance depletion (94% of Fe is depleted onto dust grains) corresponds with the peak of the distribution. As such, we implement the  $[\text{Fe}/\text{H}] = -1.25$  depletion set for all photoionization models without any adjustments.

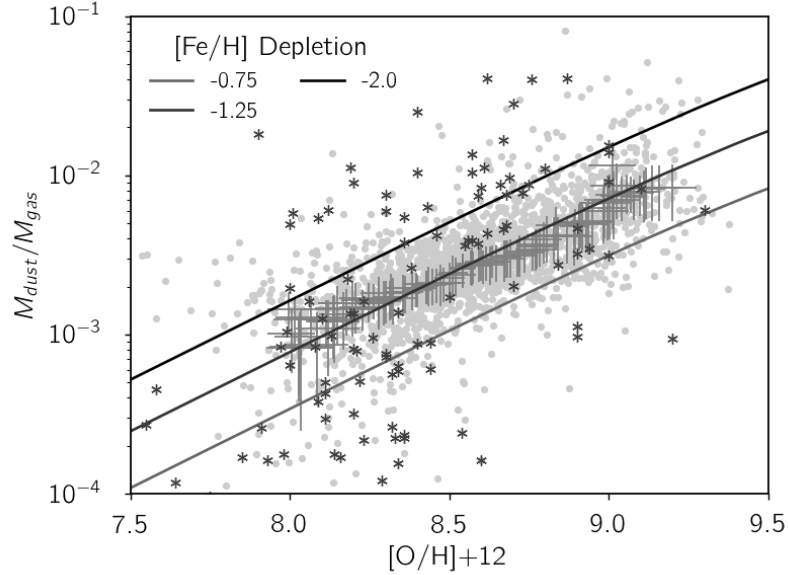


**Figure 5.6:** Dust-to-gas ratios vs. abundance for our sample of star-forming galaxies (light gray dots) binned with respect to line ratios and locus position (gray error bars). Lines represent dust-to-gas ratios as a function of chemical abundance for constant depletion rates from Jenkins (2014) applied to the Nicholls et al. (2017) Galactic Concordance. For comparison, values published in Lisenfeld and Ferrara (1998), Engelbracht et al. (2008), and Galametz et al. (2011).

While we do not account for grain destruction, we choose to exclude polycyclic

aromatic hydrocarbons from the model with the assumption that they are completely destroyed by the intense ionizing radiation from the AGN central engine (e.g., Groves et al. 2004a, Dopita et al. 2013). Following Mathis, Rumpl, and Nordsieck (1977), we implement a power law grain size distribution with an index of  $-3.5$  such that the number of grains with radius  $a$  are determined by

$$N(a) = ka^{-3.5} \quad (5.17)$$

where  $k$  is given by the ratio of dust to gas number densities. The minimum grain sizes are set to  $50 \text{ \AA}$  and  $100 \text{ \AA}$  for graphites and silicates, respectively, while the maximum for both is set to  $2500 \text{ \AA}$  with the assumption that any larger grains are destroyed by the ionizing continuum (see Groves et al. 2004a).

## 5.7 Additional Parameters

In order to determine the dust-to-gas ratio, we have to compute the optical depth from the Calzetti extinction law (see Equation 5.14). Explorations by Nicholls et al. (2014) suggest that variations in optical depth account for outliers in the abundance cooling sequence, particularly at low metallicities. We find that 131 (6.0%) of our HII sample have  $\tau < 100$ , all but three of which have  $[\text{O}/\text{H}] + 12 < 8.5$ . As we anticipate solutions which are primarily solar or super-solar, we implement the optically thick case where  $\tau \rightarrow \infty$ .

Nicholls et al. (2012) and Dopita et al. (2013) suggest a  $\kappa$ -distribution model for the kinetic energy distribution of the electron gas due to driving from the ionizing source, preventing the system from maintaining thermal equilibrium. However, the classical Maxwell-Boltzmann energy distribution ( $\kappa \rightarrow \infty$ ) is still a successful predictor of the trends between various observables (e.g. Figure 14 in Nicholls

et al. 2014, and discussion in Dopita et al. 2016), which we speculate is due to the much higher collision rates between electrons in HII and AGN regions as compared to the local ISM or solar nebula.

## 5.8 Ionizing Continuum

We utilize the AGN multicolored accretion disk spectrum model described by Done et al. (2012) and Jin et al. (2012a,b,c) as implemented by the `OPTXAGNF` code from Thomas et al. (2016). Based on comparisons of photoionization models with IFU observations of Seyfert-star-forming composites by Dopita et al. (2014) and Davies et al. (2016a), we use weights of 0.5 and 0.2 for the soft X-ray cool inverse-Compton scattering and hard X-ray hot inverse Compton scattering, respectively, relative to the disk spectrum weight of unity (see Figure 5.7). In keeping with a plethora of AGN studies, we set the mass accretion rate to 10% of the Eddington limit, which primarily affects the luminosity, and the power law index for coronal inverse-Compton scattering is set to  $\Gamma = -1.8$ , which ultimately impacts the size of the transition zone. For details on additional assumptions such as coronal radius and black hole rotation rate, see Thomas et al. (2016).

We implement this model AGN spectrum for a black hole mass of  $10^7 M_\odot$ . To determine the bolometric source luminosity, we use the canonical relation between turbulent dissipation of kinetic energy and luminosity of the disk:

$$L_{bol} = \frac{GM_{BH}\dot{m}}{2r_0} \quad (5.18)$$

where  $M_{BH}$  is the black hole mass,  $\dot{m}$  is the mass accretion rate, and  $r_0$  is the inner disk radius (Pringle 1981). We set  $r_0$  equal to the innermost stable circular orbit (ISCO) for a Schwarzschild black hole ( $r_0 = 3r_s$ ) and the accretion efficiency

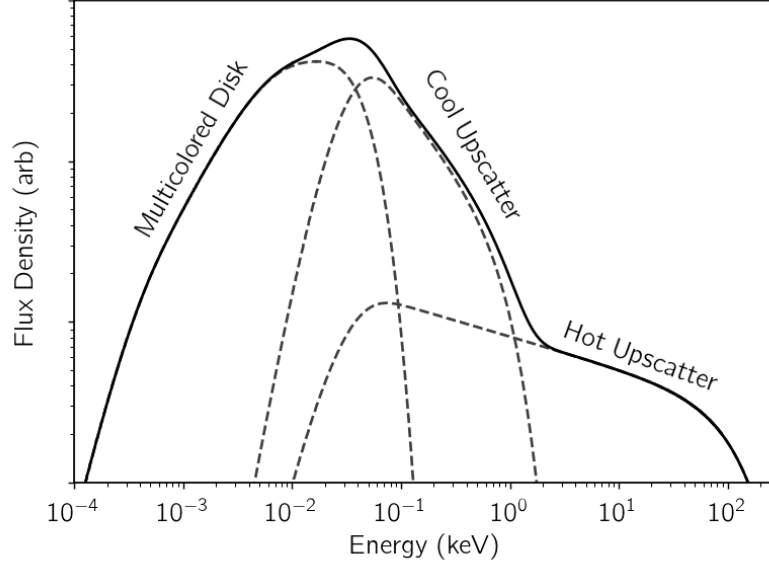


**Figure 5.7:** Model AGN spectrum for a black hole mass of  $10^7 M_\odot$  with cool and hot inverse-Compton scattering components.

to that of a disk around a Schwarzschild black hole ( $\eta = 0.06$ ), so for the assumed accretion rate of 10%, the bolometric luminosity is

$$L_{bol} = 10^{-4} \frac{GM_{BH}m_p c}{2\sigma_T} \approx 0.2515 \frac{\text{erg}}{\text{s}} \left( \frac{M_{BH}}{\text{g}} \right) \quad (5.19)$$

with  $m_p$  being the mass of a proton,  $c$  the speed of light, and  $\sigma_T$  the Thomson scattering cross section (Shakura and Sunyaev 1973). For a black hole mass of  $10^7 M_\odot$ , this gives  $\log_{10} L_{bol} = 44.242 \text{ erg s}^{-1}$ .

Explorations in parameter space by Thomas et al. (2016) demonstrate that the slope of the ionizing continuum can have a dramatic affect on the partially-ionized region of the NLR. By varying the black hole mass from  $10^6$  to  $10^9 M_\odot$ , we produce a similar effect, which can be explained by shifting of the peak of the multi-colored black body in response to the maximum temperature of the disk at the ISCO.

To compute model NLR flux ratios from nebulae at different distances from the ionizing source, we compute spherically symmetric models using the photoionization code **MAPPINGS V** (Sutherland and Dopita 2017) over a logarithmic range of the ionization parameter,  $U$ , given by

$$U = \frac{Q}{4\pi r_{neb}^2 n c} \quad (5.20)$$

where  $n \approx n_e$  is the particle density,  $c$  is the speed of light,  $r_{neb}$  is the distance of the model ISM cloud from the ionizing source, and  $Q$  is the number of photons in the source spectrum capable of ionizing neutral hydrogen each second (i.e., with  $\nu \geq \nu_0 = 3.288 \times 10^{15}$  Hz). This photon “rate” is given by

$$Q = \int_{\nu_0}^{\infty} \frac{L_\nu}{h\nu} d\nu, \quad (5.21)$$

which, for the luminosity and spectrum assumed above, is  $\sim 10^{54} \text{ s}^{-1}$ . For a fixed ionizing spectrum, bolometric luminosity, and electron density, a broad range of  $U$  corresponds directly to a broad range of cloud distances from the ionizing source, allowing us to explore the impact that geometry might have on a single-aperture spectroscopic observation over several orders of magnitude in cloud distance. As such, we choose a range of  $\log U \in [-4, 0]$  to cover the full range of possible NLR sizes of tens of parsecs out to a few kiloparsecs.

## Chapter 6

### The Purpose Holds

---

There lies the port; the vessel puffs her sail:  
There gloom the dark, broad seas.  
The lights begin to twinkle from the rocks:  
The long day wanes: the slow moon climbs: the deep  
Moans round with many voices. Come, my friends,  
'T is not too late to seek a newer world.  
Push off, and sitting well in order smite  
The sounding furrows; for my purpose holds  
To sail beyond the sunset, and the baths  
Of all the western stars

— “Ulysses”, Alfred Lord Tennyson

---

In their 2016a paper, Davies et al. put forward the concept of a “hybrid mixing sequence”. They compared the Seyfert-like spaxels from “pure” AGN and from composite objects hosting an AGN against a grid of photoionization models with a range of chemical abundances and degrees of ionization. In doing so, they demonstrated that the NLR follows a sequence of changing emission line ratios associated with photoionization models of a single metallicity and ionization parameters ranging over several orders of magnitude. Visually, this appears as a cusp or kink in the mixing sequence, typically on the Seyfert side of the Ke01 demarcation in the principal BPT diagnostic diagrams. In our A sample, NGC 613 exhibits this feature in the distribution of its flux ratios at  $\log_{10}[\text{OIII}]/\text{H}\beta \approx -0.1$  and  $\log_{10}[\text{NII}]/\text{H}\alpha \approx 0.0$ , which is visible in Figure 4.6 in Chapter 4 roughly where

the full spaxel flux ratio distribution diverges from the simple mixing prediction. This NLR ionization sequence can account for the discrepancy between our simple model predictions and the observed spaxels.

We propose that this NLR ionization sequence is due to an effect we refer to as “geometric dilution”. First, consider optically-thin clouds distributed uniformly in a spherical shell of some radius  $r_{neb}$  and some infinitesimal width. All else being equal, this shell will produce less total emission-line flux than a shell of identical composition and thickness but larger inner radius because the initial shell has less total line-emitting gas. Second, the intrinsic emission-line flux per unit volume of NLR cloud depends on the distance of that cloud from the ionizing source due to the inverse-square law effect on the ionizing flux. Third, in a single aperture spectroscopic observation, the observed flux is a superposition of fluxes from the spherical shells composing the NLR. Given these premises are sound, it stands to reason that a single aperture observation is a volume-weighted integration of emission-line fluxes of varying ionization parameter.

To demonstrate this, we use the empirically-motivated photoionization models described in Chapter 5 to simulate single aperture observations of a spherically symmetric, unextended NLR to reproduce our predicted AGN positions. Then, we demonstrate this effect in two “pure” AGN with ENLR to verify that our hypothesis is consistent with AGN uncontaminated by star formation. With confirmation that our dilution model is correct, we incorporate the fluxes predicted by photoionization models into the composite mixing sequence.

## 6.1 Simulating Single-Aperture Observations

While each photoionization model in Chapter 5 has been computed for a spherical shell surrounding the photoionization source, our goal in demonstrating geo-



metric dilution of the NLR emission-line fluxes requires combining these models to “integrate” the entire volume of the spherical nebula. We integrate by populating a hollow sphere with clouds uniformly distributed with respect to shell radius  $r_{neb} \propto U^{-1/2}$  within the sphere (inherently, this indicates the number of clouds is proportional to  $r_{neb}$ ). Because the photoionization model already accounts for the full volumetric distribution of matter in the shell when predicting the observed emission-line flux, a radially uniform distribution of clouds is appropriate for simulating a superposition of clouds within the spectral aperture.

Each cloud is assigned volume-weighted emission-line fluxes predicted by the photoionization model for that particular radius. We do this by interpolating the model emission-line fluxes with respect to  $\log U$  using the function `splrep` from the module `scipy.interpolate` with a cubic spline forced to intersect each of the 17 total model fluxes for each emission line. Each flux spline is evaluated at the cloud’s distance using the `scipy.interpolate` function `splev` to determine the flux “emitted” by the cloud. With volume-weighted line fluxes assigned to all the clouds in our model NLR, we simulate a single-aperture observation by summing up all the fluxes from clouds contained within a minimum  $\log U$  (corresponding to a maximum radius) ranging from  $\log U_{min} = -1.5$  to  $\log U_{min} = -4$ . As a result of this volume-weighted integration, the observed flux ratios in the BPT diagram lie on the lower right end of the distribution of flux ratios predicted by photoionization models of a given metallicity (see Figure 6.1).

To demonstrate this effect observationally, we return to the S7 IFU observations. This time, we examine the spatially resolved spectroscopy of the ENLR of two “pure” AGN: NGC 2992 and NGC 3281. These two galaxies are particularly useful as demonstrations of geometric dilution because the spatially resolved flux ratios correspond to an implied range of cloud distances from the ionizing source.

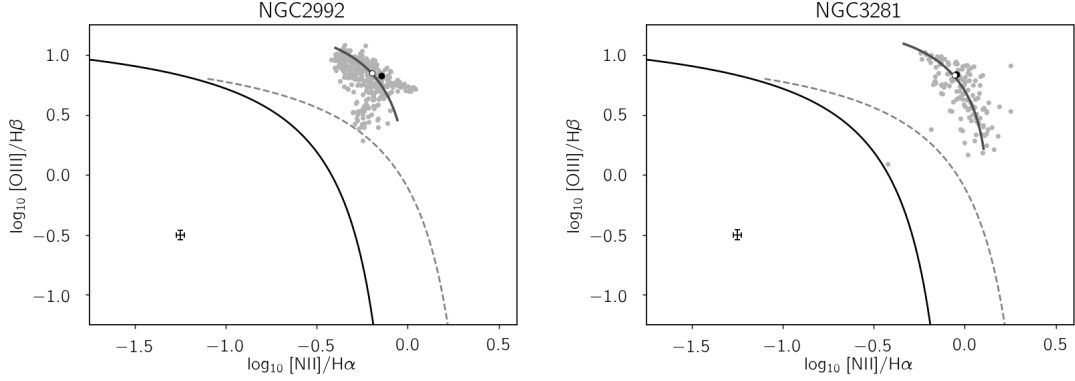


**Figure 6.1:** Flux ratios for spaxels with well-detected fluxes (light grey dots) and summed-flux ratios (filled circles) for NGC 2992 (*left*) and NGC 3281 (*right*). Photoionization model flux ratios which best describe the distribution of spaxels (dark grey lines) with simulated dilute flux ratios (open circles). Error bar represents the characteristic  $1\sigma$  uncertainties in spaxel flux ratios.

From each spaxel, we cull the relevant emission line fluxes in the cases where the flux is detected at  $F_\lambda \sigma_{F_\lambda}^{-1} > 3$ . We then sum these fluxes to simulate a single-aperture observation and compare the summed-flux ratios to the distribution of spaxel flux ratios in the primary BPT diagnostic in Figure 6.1.

As an assessment of our dilution model, we select for each galaxy a set of photoionization model flux ratios which compose a single-abundance dilution sequence which bisects the observed distribution of spaxel flux ratios. We limit the range of  $\log U$  so that the dilution sequence corresponds to the upper and lower limits of the spaxel flux ratios. We then simulate a single aperture observation as describe above using the metallicity and ionization parameters implied by the IFU data. We plot both the photoionization model dilution sequence and the simulated geometrically dilute flux ratios against the spaxel and summed-flux ratios in Figure 6.1. Both approaches produce the same results: dilute flux ratios which lie within their respective distributions of flux ratios and which are separated from one another by less than 0.1 dex.

The strong agreement between the model dilute flux ratios and the observed summed-flux ratios shown in Figure 6.1 demonstrates that our framework for interpreting single-aperture flux ratios of “pure” AGN is correct. In the context of the mixing sequence, this suggests that the predicted flux ratios for the AGN component of the composite represent a geometrically dilute sum of NLR fluxes, each of which depend on ionization parameter. Decomposing the AGN flux ratios into a sequence of flux ratios corresponding to different values of  $\log U$  will allow us to appropriately incorporate the AGN component into the mixing sequence. However, this would require knowing the range of ionization parameters which correspond to the observed dilute flux ratios in order to construct the appropriate dilution sequence.

## 6.2 Effective Ionization Parameter

Because of the superposition of clouds in the spectroscopic aperture, the true distribution of ionization parameters across the NLR are not the value of  $\log U$  we would compute given the flux ratios observed in a single aperture spectrum or predicted by the simple mixing model. This observed, or “effective”, ionization parameter is instead representative of the distribution of clouds in the nebula as well as the nebula’s maximum outer radius, which corresponds to a minimum ionization parameter. To establish a model-dependent relation between  $\log U_{eff}$  and  $\log U_{min}$ , we compare the simulated single-aperture summed-flux ratios to the single-shell flux ratios originally predicted by the photoionization models. We compute the effective ionization parameter by finding the root value of  $\log U$  which minimizes the difference between the single-shell and simulated single-aperture flux ratios. This means that  $\log U_{eff}$ , as we compute it, is the ionization parameter which would characterize the observed flux ratios if they were not geometrically

diluted but rather emanating from a single-shell nebula.

In the initial setup of the simulated single-aperture observation, we defined  $\log U_{min}$  in order to distribute clouds across the entire NLR. As a result, we know the true  $\log U_{min}$  which corresponds to each value of  $\log U_{eff}$  and compute the difference  $\Delta \log U$  between the two. In Figure 6.2, we show  $\Delta \log U$  for a NLR of gas-phase metallicity  $[\text{O}/\text{H}] + 12 = 8.7$  for the range of nebula radii within which the root-finding algorithm converges for each flux ratio. We describe the relation between  $\log U_{eff}$  and  $\Delta \log U$  for each flux ratio with a fifth-order polynomial fit to the model points using the `numpy` function `polyfit`. Using this, we can extrapolate beyond the range of  $\log U_{eff}$  and  $\log U_{min}$  values covered by our simulation, as shown in Figure 6.2.

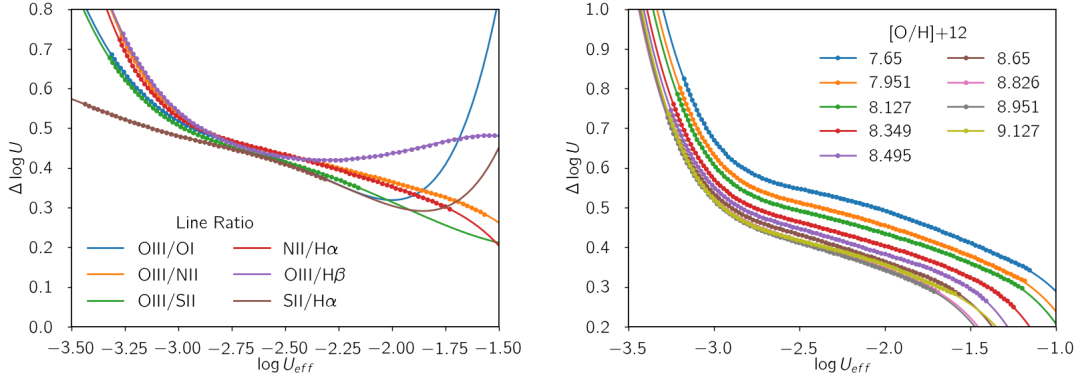


**Figure 6.2:** *Left:*  $\Delta \log U$  according to various line ratios (colors) for model NLRs of gas phase metallicity  $[\text{O}/\text{H}] + 12 = 8.7$  ( $\approx Z_{\odot}$ ) with a range of sizes (dots) as fit by fifth-order polynomials (lines). *Right:*  $\Delta \log U$  according to  $\log_{10}[(\text{[OIII]}/\text{H}\beta)/(\text{[NII]}/\text{H}\alpha)^{-1}]$  over a range of abundances.

We consider the  $\log U_{min} - \Delta \log U$  relation implied by the  $([\text{OIII}]/\text{H}\beta)/([\text{NII}]/\text{H}\alpha)$  flux ratio ratio shown in Figure 6.2 for three reasons: (a) the emission lines are frequently well-detected, (b) these flux ratios are inherently reddening insensitive, and (c) we have already computed the  $[\text{NII}]/\text{H}\alpha$  and  $[\text{OIII}]/\text{H}\beta$  flux ratios for the AGN component in our composite decomposition method. As shown in Figure

6.2, the parameters for the fifth-order polynomial descriptions given in Table 6.1 change as a function of metallicity. We apply a quadratic spline to the parameters of the best-fit polynomials over the range of relative oxygen abundances, so that, for a characteristic metallicity, we can determine  $\Delta \log U$  and recover the range of undiluted NLR flux ratios.

**Table 6.1:** Coefficients for fifth-order polynomial fits to the  $[\text{OIII}]/\text{H}\beta$  /  $[\text{NII}]/\text{H}\alpha$  estimate of  $\Delta \log U$  over the range of model NLR metallicities.

$[\text{O}/\text{H}]+12$	$a_1$	$a_2$	$a_3$	$a_4$	$a_5$	$a_6$
7.65	-0.114	-1.079	-4.015	-7.366	-6.853	-2.248
7.951	-0.12	-1.174	-4.517	-8.592	-8.259	-2.892
8.127	-0.121	-1.2	-4.695	-9.108	-8.923	-3.226
8.349	-0.144	-1.496	-6.176	-12.688	-13.14	-5.199
8.495	-0.185	-2.014	-8.72	-18.801	-20.34	-8.551
8.65	-0.193	-2.139	-9.431	-20.746	-22.933	-9.931
8.826	-0.196	-2.19	-9.789	-21.897	-24.683	-10.973
8.951	-0.202	-2.267	-10.166	-22.835	-25.864	-11.574
9.127	-0.163	-1.74	-7.4	-15.731	-16.905	-7.112

### 6.3 Dilute Mixing Sequence

As anticipated from Groves et al. (2004a,b), the single-aperture diluted flux ratios cover a wide range on the BPT diagnostic diagram ( $\sim 2$  dex) due to changes in chemical abundance. It is reasonable to assume, given studies of nuclear H II region abundances coincident with Seyferts (Evans and Dopita 1987; Storchi-Bergman et al. 1998; Ho et al. 2015), that the oxygen abundance associated with the starburst component of a composite would be similar to that of the NLR. Following from this premise, we take the median and root-median-square of the  $[\text{O}/\text{H}]+12$  values in the HII locus position bins described in Chapter 3.

Using this characteristic metallicity, we select the photoionization model flux ratios characteristic of the NLR associated with the composite candidate by

quadratically interpolating over the line fluxes from the photoionization models with respect to  $[\text{O}/\text{H}]+12$  at each model value of  $\log U$ . We then evaluate the interpolation for the chemical abundance implied by the H II region. This produces a sequence of model flux ratios which vary exclusively with respect to ionization parameter. Since  $Q$  and  $n$  are fixed, this sequence demonstrates changes in flux ratio as a result of geometric dilution of the ionizing flux<sup>1</sup>. It stands to reason, then, that the AGN line ratios contributing to composite emission of any given point along the mixing sequence depend on distance from the photoionizing source in addition to the AGN fraction.

From the dilution sequence inferred from the metallicity, we can estimate  $\log U_{min}$  of the dilution sequence by comparing the predicted single-aperture AGN component to the range of flux ratios to determine  $\log U_{eff}$  and evaluating the appropriate polynomial to obtain  $\Delta \log U$ . To compute the mixing sequence, we match  $\log U_{min}$  with an AGN fraction of zero and increase  $\log U$  incrementally in dex with linear increments of  $f_{AGN}$  until  $\log U = -2.75$  at  $f_{AGN} = 1^2$ . To construct the dilute mixing sequence, we adjust Equation 2.10 so that  $F_{\lambda,AGN}$  now varies as a function of  $\log U$ , which is itself a function of  $f_{AGN}$  as a result of our forced coupling. Variations in  $\log U_{min}$  have significant influence on the shape of the mixing sequence, introducing a range of solutions spanning as much as a 0.4 dex parallel to the Ka03 demarcation in the primary BPT diagnostic diagram (see Figure 6.3). At super-solar metallicities and  $\log U_{min} < -3.5$ , the

---

<sup>1</sup>While this is, in a way, a “dilution sequence”, it is not to be confused with the geometric dilution of a single-aperture observation described previously, which is due to both the coupling of the inverse square law dilution of the ionizing flux and the volumetric dilution of the emitted line flux.

<sup>2</sup>We recognize that this assumption is somewhat arbitrary and begs further investigation. At present, there is no foreseen empirical constraint on this value, but the fraction- $\log U$  coupling of our dilute mixing sequence requires a maximum  $\log U$ . This chosen value is not uncharacteristic of many NLRs, including the two ENLR shown in Figure 6.1 and reliably provides viable solutions, as shown in Figure 6.3.

sequences traverse part of the LINER regime of the primary BPT diagnostic, perhaps explaining the “transition” nuclei of HFS93.

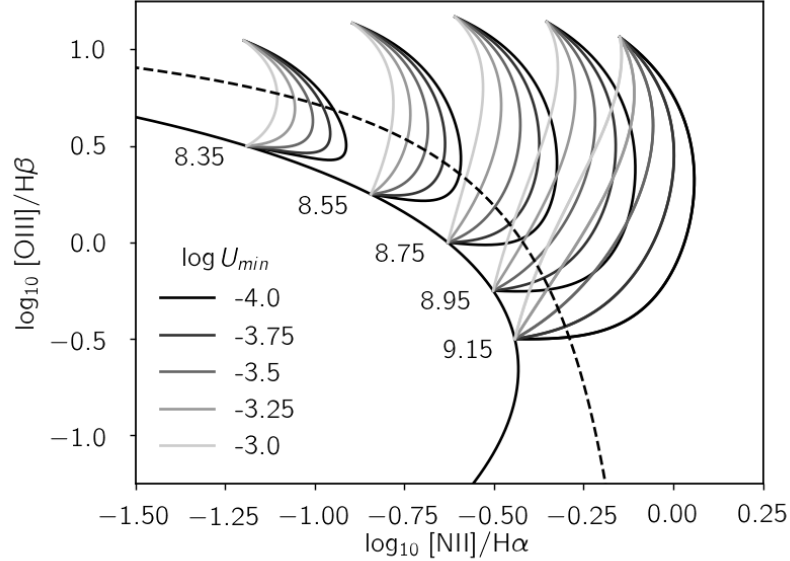


**Figure 6.3:** Mixing sequences for a range of oxygen abundances matched to the appropriate dilution sequence and locus position. The mixing sequences for each metallicity are computed over a range of  $\log U_{min} \in [-4, -3]$ .

## 6.4 Second Coming

We apply this new metallicity-based component of the method to the A sample of composite candidates and show the results in Figure 6.4. Even at first glance, it is evident that the predicted dilute mixing sequences for IC 5169 and NGC 613 are far better at recovering the entire distribution of spaxel flux ratios, not only those within the aperture. What Figure 6.4 also demonstrates is that the remaining four objects are not well characterized by this more complex mixing model.

In light of the two obvious successful predictions, we obtain deeper insight into the true nature of composites. First, the hypothesis of simple mixing seeming fails

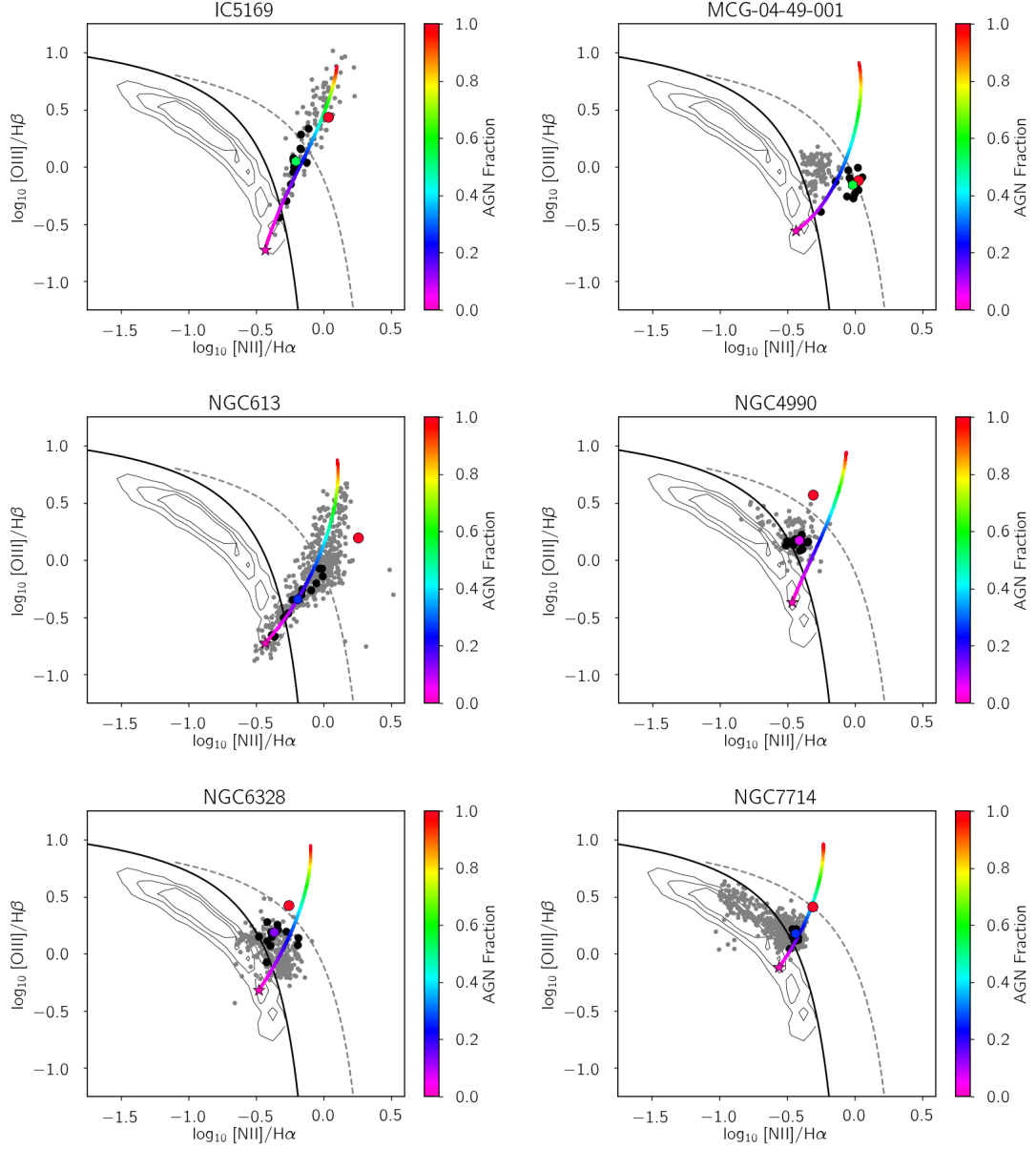


**Figure 6.4:** Dilute composite mixing model for galaxies in the A sample. All other symbols as in Figure 4.6.

to properly model the flux ratios from spaxels outside the aperture, suggesting the environment of truly composite galactic nuclei is more complex than previously thought. What's more, the extent of the NLR, changes in ionization structure of NLR gas as a function of  $\log U$ , and the geometric dilution of emission line



fluxes in the NLR have a significant affect on the observed mixing sequence. One might take the success of the more dilution mixing model in predicting the IFU flux ratios to mean the simple mixing is no longer valid. However, the AGN flux ratios predicted by the simple mixing model in both cases are likely the dilute NLR flux ratios, which suggests that the simple mixing sequence is the expected distribution of composite flux ratios between a starburst and an already diluted AGN. Accounting for this dilution, as we have discussed here, brings the simple mixing model into agreement with the observations.

The consistent failure of the composite hypothesis for starburst galaxy NGC 7714 demonstrates that a number of composite candidates may simply be objects that exhibit chemically enriched star formation or possess a stellar population which produces a harder, more intense ionizing spectrum than is typical of OB associations in H II regions. Such an interpretation of composites is not outside the realm of possibility because any objects which reside below the Ke01 [NII]/H $\alpha$  demarcation can be theoretically described as starbursts. Considering Ke06 found that many composite candidates fall in the H II locus in the other two BPT diagnostics, this position is not unreasonable.

What remains to be understood is the nature of the remaining galaxies. According to the predictions by our linear mixing model, the ionizing mechanism(s) responsible for producing the observed ion species is unclear. It is possible that NGC 4990 and NGC 6328 are also nitrogen-rich starbursts; however, we do not currently have an empirical method for demonstrating this quantitatively. MCG -04-49-001 seems more akin to the “transition” galaxies of HFS93 because of the LINER-like [NII]/H $\alpha$  flux ratios. Galactic super winds the likes of M82 and NGC 839 might account for this non-stellar component, and Rich et al. (2010) go so far as to propose a linear combination of outflow and star formation as an

---

interpretation for composite spectra. The validity of this hypothesis in the context of this object and indeed for all composites has not been thoroughly tested and in all likelihood would require analysis of additional diagnostic lines, such as  $[\text{NI}]\lambda\lambda 5198, 5200$  (Sarzi et al. 2010). Whatever the case, these three ambiguous galaxies suggest that composite galaxies may be a heterogeneous class, like LINERs.

## Chapter 7

### But After All

---

We've looked and looked, but after all where are we?  
Do we know any better where we are...  
How different from the way it ever stood?

— “The Star-Splitter”, Robert Frost

---

We have presented the predictions of our decomposition method as applied to IFU data as an assessment for testing the composite hypothesis and our technique. While significant and compelling in their own right, these results demonstrate a need for future work. First, we will consider additional empirical means with which to localize our technique’s predicted viable AGN flux ratios in the BPT diagnostic diagrams. We will then develop a means to assess the dilute mixing sequence predictions that is consistent with but independent of IFU data. We then address the B sample of S7 composite candidates with two goals: demonstration that the method developed and tested against the higher quality A sample continues to successfully reject the composite hypothesis for objects which are not composite.

After completing tests with spatially resolved spectroscopy, additional work will involve applying our technique to single-aperture surveys such as the SDSS to constrain the lower limit on the number of composite candidates which host an active MBH. Within this goal is a specific aim is to examine a subsample of composite candidates for which the He II emission line is detected. The impetus

for this particular subsample follows from discussions in SB12 about the HeII/H $\beta$  flux ratio as a diagnostic of the spectral hardness of the ionizing source. As such, we expect to see a high success rate in our decomposition predictions for composite candidates which satisfy a HeII/H $\beta$  criterion. Followup IFU spectroscopy will be necessary to test these predictions and explore the nuclear activity in composite candidates to better understand their underlying physical nature.

Once rigorously tested, our ability to determine the presence of a MBH from a single observation of a composite galaxy will have far-reaching implications. More complete information about the frequency of AGN could shed light on the poorly understood correlations between MBHs and properties of their host galaxies, most notably the  $M_{BH} - \sigma_*$  relation in which a MBH's mass is observed to be directly proportional to the velocity dispersion of stars within the host galaxy's nucleus (e.g., Ferrarese and Merritt 2000, Gültekin et al. 2009). Larger samples of confirmed MBHs can lead to better constraints on the slope of this correlation, which is not well explored for low MBH masses or low  $\sigma_*$ . The starburst component of these confirmed MBHs could offer insight into the relationship between stellar processes across the entire nucleus and AGN activity. These composites of H II and AGN emission may also have important implications for understanding the observed correlation between MBH gas accretion rate and host galaxy star-formation rate over cosmic time (e.g., Hopkins et al. 2007, Kauffmann et al. 2007, Silverman et al. 2009, Aird et al. 2010, Chen et al. 2013). The opportunity to study simultaneous star formation and MBH activity in confirmed true composite galactic nuclei could lead to a deeper understanding of the connection between these two phenomena.

The  $M_{BH} - \sigma_*$  relation and the correlation of star formation and MBH accretion rates might suggest that a MBH somehow evolves in tandem with its host,

although this is not well understood and often contested. Several studies, such as Greene, Ho, and Barth (2008) and Xiao et al. (2011), demonstrate that the coevolution relationship is tenuous for IMBHs in dwarf galaxies, perhaps indicating that the central BH is decoupled from its host except in instances of galactic mergers. Volonteri et al. (2016), among others, maintain that processes independent of mergers are key to understanding the scatter in MBH–galaxy mass correlations. A larger population of BH–starburst composites could shed light on this coevolution or lack thereof, particularly in the case of dwarf galaxies.

While application of our decomposition method to composite galaxy samples would provide insight in AGN–host co-evolution, perhaps an even more compelling result would be the vastly improved MBH census. Dwarf galaxies have undergone relatively little evolution over the lifetime of the universe and are thus relics of an earlier cosmic epoch. The frequency at which IMBHs occur in dwarf galaxies, the so-called “occupation fraction”, sheds light on the origin of MBHs. A better estimate of the frequency at which local IMBHs occur in dwarf galaxies would provide a constraint of greater significance on the occupation fraction, which is crucial to determining the formation mechanism of the primordial seeds for today’s supermassive black holes (SMBHs, e.g., Volonteri 2010, Devecchi et al. 2012, Habouzit et al. 2017).

Of course, this is not an exhaustive list of the impact our decomposition method could have; however, what we have presented here is substantial enough to motivate future work in both confirming our technique and applying it to large surveys in order to answer key scientific questions about the origins, evolution, and coevolution of MBHs.

---

Go, little book,  
out of this house and into the world,

carriage made of paper rolling toward town  
bearing a single passenger  
beyond the reach of this jitter pen,  
far from the desk and the nosy gooseneck lamp.

It is time to decamp,  
put on a jacket and venture outside,  
time to be regarded by other eyes,  
bound to be held in foreign hands.

So, off you go, infants of the brain,  
with a wave and some bits of fatherly advice:

stay out as late as you like,  
don't bother to call or write  
and talk to as many strangers as you can.

— “Envoy”, Billy Collins

---

## Bibliography

- Abazajian, K., et al. 2009. ApJS 182, 543.
- Acosta-Pulido, J., et al. 1990. ApJ 365, 119A.
- Aihara, H., et al. 2011. ApJS 193, 29.
- Aird, J., et al. 2010. MNRAS 401, 2531.
- Allen, M., et al. 2008, ApJS, 178, 20
- Baldwin, J., Phillips, M., and Terlevich, R. 1981. PASP 93, 5.
- Bär, R., et al. 2017. MNRAS 466, 2879.
- Barth, A., Greene, J., & Ho, L. 2005. ApJ 619, L151.
- Bennert, N., et al. 2006. A&A 456, 953.
- Berg, D., et al. 2012. ApJ 754, 98.
- Binette, L. et al. 1994. A&A 292, 13.
- Binette, L. et al. 2012. A&A 547, A29.
- Bresolin, F., et al. 2005. A&A 441, 981.
- Bresolin, F., et al. 2009. ApJ 700, 309.
- Bresolin, F., et al. 2016. ApJ 830, 64.
- Brinchmann, J., Kunth, D., and Durret, F. 2008. AA 485, 657.
- Brinchmann, J., Pettini, M., and Charlot, S. 2008. MNRAS 385, 769.
- Brinchmann, J., et al. 2013. MNRAS 432, 211B.
- Calzetti, D. 2001. PASP 113, 790.
- Cappellari, M. and Emsellem, E. 2004. PASP 116, 138C.
- Castellanos, M., Díaz, Á., and Terlevich, E. 2002. MNRAS 329, 315.
- Chen, C.-T., et al. 2013. ApJ 773, 3.
- Cid Fernandes, R., et al. 2010. MNRAS 403, 1036.

- Davies, R., et al. 2007. ApJ 671, 1388.
- Davies, R., et al. 2014a. MNRAS 439, 3835.
- Davies, R., et al. 2014b. MNRAS 444, 3961.
- Davies, R., et al. 2016a. ApJ 824, 50.
- Davies, R., et al. 2016b. MNRAS 462, 1616.
- Davies, R., et al. 2017. MNRAS 470, 4974.
- Del Zanna, G. et al. 2015. A&A 582A, 56D.
- Dere, K. P., et al. 1997. A&AS 125, 149D.
- Devecchi, B., et al. 2012. MNRAS 421, 1465.
- Díaz, Á., et al. 2007. MNRAS 382, 251.
- Done, C., et al. 2012. MNRAS 420, 1848.
- Dopita, M., et al. 2002. ApJ 572, 753.
- Dopita, M., et al. 2013. ApJS 208, 10D.
- Dopita, M., et al. 2014. A&A 566A, 41D.
- Dopita, M., et al. 2015. IAU Symp 309, 200.
- Dopita, M., and Sutherland, R. 2017, ApJS, 229, 35
- Draine, B. 2011. *Physics of the Interstellar and Intergalactic Medium*.
- Dufour, P., et al. 2017. ASPC 509, 3D.
- Emsellem, E., et al. 2004. MNRAS 352, 721E.
- Engelbracht, C., et al. 2008. ApJ 678, 804E.
- Eracleous, M., Hwang, J, and Flohic, H. 2010. ApJ 711, 796.
- Evans, I. and Dopita, M. 1987. ApJ 319, 662.
- Fath, E. 1909. LicOB 149, 71.
- Ferland, G. and Netzer, H. 1983. ApJ 264, 105.
- Ferrarese, L. and Merritt, D. 2000. ApJ 539, L5.



- Filippenko, A. 2003. “LINERs and their Physical Mechanisms”. In *Active Galactic Nuclei: From Central Engine to Host Galaxy*. 290, 369F. Eds. Collin, S., Combes, F., and Shlosman, I. ASPCS(AGNFCEHG).
- Fukugita, M., et al. 1996. AJ 111, 4.
- Galliano, F., Dwek, E., and Chanial, P. 2008. ApJ 672, 214.
- Galametz, M., et al. 2011. A&A 532, A56.
- Greene, J. & Ho, L. 2004. ApJ 610, 722.
- Greene, J. & Ho, L. 2007. ApJ 670, 920.
- Greene, J., Ho, L., and Barth, A. 2008. ApJ 688, 159.
- Groves, B., et al. 2004a. ApJS 153, 9.
- Groves, B., et al. 2004b. ApJS 153, 75.
- Groves, B., et al. 2006. MNRAS 371, 1559.
- Gültiken, K. et al. 2009. ApJ 698, 198.
- Güver, T, and Özel, F. 2009. MNRAS 400, 2050.
- Habouzit, M., et al. 2017. MNRAS 468, 3935.
- Heckman, T. 1980. A&A 87, 152.
- Heckman, T., et al. 1989. ApJ 338, 48.
- Hill, T., et al. 2001. AJ 121, 128.
- Hillier, D. and Lanz, T. 2001, ASPC, 247, 343.
- Hirschauer, A., et al. 2015. AJ 150, 71.
- Ho, L., Filippenko, A., and Sargent, W. 1993. ApJ 417, 63.
- Ho, L., Filippenko, A., and Sargent, W. 1997. ApJS 112, 315.
- Ho, I-T., et al. 2015. MNRAS 448, 2030.
- Ho, I-T., et al. 2016. Ap& SS 361, 280H.
- Hopkins, P., et al. 2007. ApJ 659, 976.
- Izotov, Y. et al. 2006. A&A 448, 955.

- Jenkins, E. 2013. “Depletions of Elements from the Gas Phase: A Guide on Dust Compositions”. In LCDU2013, 005, Eds. Kemper, C., et al.. PoS.
- Jin, C., et al. 2012. MNRAS 420, 1825.
- Jin, C., Ward, M., and Done, C. 2012. MNRAS 422, 3268.
- Jin, C., Ward, M., and Done, C. 2012. MNRAS 425, 907.
- Kauffmann, G., et al. 2003. MNRAS 1055, 77.
- Kauffmann, G., et al. 2007. ApJS 173, 357.
- Kawasaki, K. et al. 2017. ApJ 842, 44K.
- Kennicutt, R. 1998. 498, 541K.
- Kewley, L., et al. 2001. ApJ 556, 121.
- Kewley, L., & Dopita, M. 2002. ApJS 142, 35.
- Kewley, L., Jansen, R., and Geller, M. 2005. PASP 117, 227K.
- Kewley, L., et al. 2006. MNRAS 961, 76.
- Kewley, L. & Ellison, S. 2008. ApJ 681, 1183.
- Kewley, L., et al. 2013. ApJ 74, 100K.
- Kirkpatrick, A., et al. 2015. ApJ 814, 9.
- Kormendy, R. and Richstone, K. 1995. ARA&A 33, 581.
- Kormendy, R. and Ho, L. 2013. ARA&A 51, 511.
- Koss, M., et al. 2017. ApJ 850, 74.
- Kotulla, R., et al. 2009. MNRAS 396, 462.
- Kroupa, P. 2002. Science 295, 82.
- Leitherer et al. 2014. ApJS 212, 14.
- Lisenfeld, U. and Ferrara, A. 1998. ApJ 496, 1.
- López-Sánchez, A. R. and Esteban, C. 2009. A&A 508, 615.
- Ludwig, R., et al. 2012. ApJ 756, 51.
- Maraston, C. and Strömbäck, G. 2011. MNRAS 418, 2785.

- Mathis, J., Rumpl, W., & Nordsieck, K. 1977. ApJ 217, 425M.
- Moran et al. 2014. AJ 148, 136M.
- Nicholls, et al. 2012. ApJ 752, 148.
- Nicholls, D., et al. 2014. ApJ, 790, 75
- Nicholls, D., et al. 2017. MNRAS, 466, 4403
- Oh, K., et al. 2011. ApJS 195, 13O.
- Oke, J. and Gunn, J. 1983. ApJ 266, 713.
- Osterbrock, D., and Ferland, G. 2006. *Astrophysics of Gaseous Nebulae and Active Galactic Nuclei*.
- Pettini, M. and Pagel, B. 2004. MNRAS 348, L59.
- Penston, M. and Fosbury, R. 1978. MNRAS 183, 479.
- Popping, G., Somerville, R., and Galametz, M. 2017. MNRAS 471, 3152.
- Pringle. 1981. ARA&A 19, 137P.
- Rauch, T. 2003. A&A 403, 709.
- Reines, A., Greene, J., & Geha, M. 2013. ApJ 775, 116R.
- Sánchez, S., et al. 2012. A&A 538A, 8S.
- Sartori, L., et al. 2015. MNRAS 454, 3722.
- Sarzi, M., et al. 2006. MNRAS 366, 1151.
- Sarzi, M., et al. 2010. MNRAS 402, 2187.
- Seth, A., et al. 2008. ApJ 678, 116.
- Seyfert, C. 1943. ApJ 97, 28S.
- Shakura, and Sunyaev. 1973.
- Shirazi, M. and Brinchmann, J. 2012. MNRAS 421, 1043.
- Silverman, J., et al. 2009. ApJ 696, 396.
- Spitzer, L. 1949. ApJ 109, 337S.
- Stasińska, G. 1980. A&A 84, 320.

- Stasińska, G. 2005. A&A 434, 507.
- Storchi-Bergmann, T., et al. 1998. AJ 115, 909.
- Rich, J., et al. 2010, ApJ, 721, 505
- Tadhunter, C. and Tsvetanov, Z. 1989. *Nature* 341, 422.
- Thomas, D., et al. 2013. MNRAS 431, 1383.
- Thomas, A., et al. 2016. ApJ 833, 266T.
- Thomas, A., et al. 2017. ApJS 232, 11T.
- Toribio San Cipriano, L., et al. 2017. MNRAS 467, 3759.
- Trump, J., et al. 2015. ApJ 811, 26.
- Unger, S., et al. 1987. MNRAS 228, 671U.
- van Zee, L., et al. 1998. AJ 116, 2805.
- van Zee, L. and Haynes, M. 2006. ApJ 636, 214.
- Vazdekis, A., et al. 2015. MNRAS 449, 1177V.
- Veilleux, S. and Osterbrock, D. 1987. ApJS 63, 295.
- Verner, D., et al. 1996. ApJ 465, 487V.
- Véron, P., et al. 1981. A&A 97, 71.
- Volonteri, M. 2010. AAR 18, 279.
- Volonteri, M., et al. 2016. MNRAS 460, 2979.
- Wilson, A., and Heckman, T. 1985. In *Astrophysics of Active Galaxies and Quasistellar Objects*. Ed. Miller, J., 39. Oxford UP.
- Wilson, A., Baldwin, J., and Ulvestad, J. ApJ 291, 627W.
- Yan, R. & Blanton, M. 2012. ApJ 747, 61.